RSC Advances

This article can be cited before page numbers have been issued, to do this please use: K. S. Ramakrishnan, Y. Subramanian and Y. Lee, *RSC Adv.*, 2016, DOI: 10.1039/C5RA23503K.

ROYAL SOCIETY OF CHEMISTRY

www.rsc.org/advances

View Article Online
DOI: 10.1039/C5RA23503K

Journal Name

ARTICLE

An overview of AB_2O_4- and A_2BO_4-structured negative electrodes for advanced Li-ion batteries

Received 00th January 20xx,
Accepted 00th January 20xx

DOI: 10.1039/x0xx00000x

www.rsc.org/

Subramanian Yuvaraj[a], Ramakrishnan Kalai Selvan[a]*, Yun Sung Lee[b]*

Energy-storage devices are state-of-the-art devices with many potential technical and domestic applications. Conventionally used batteries do not meet the requirements of electric or plug-in hybrid-electric vehicles due to their insufficient energy and power densities. Carbon is used for the conventional anodes of Li-ion batteries. However, the specific capacity (372 mAh g^{-1}) of a graphite electrode is not sufficient for high-power applications. Therefore, Co-, Ni-, Mn-, and Zn-based simple oxides have been investigated as anode components due to their high specific capacities (500–1000 mAh g^{-1}). Among these, Co-based anodes have demonstrated the best electrochemical performances; however, Co's high cost and toxicity limit its use as an ideal anode component. Recently, mixed-metal oxides with AB_2O_4 (*A* = Cu, Co, Ni, Mn, and Zn; *B* = Co, Mn, and Fe) and A_2BO_4 (*A* = Co, Mn, and Fe; *B* = Sn, Si, Ti, and Ge) structures have received much interest, and their electrochemical performances have been extensively studied. This type of mixed-metal oxide afford the following main advantages: they store charge through conversion as well as alloying–dealloying processes, and they exhibit higher electronic conductivities than that obtained with simple metal oxides. The above points indicate the importance of AB_2O_4- and A_2BO_4-structured materials. The present review emphasizes the recent literature on the electrochemical performance of AB_2O_4- and A_2BO_4-structured materials and their composites and feasible ways to implement these materials in Li-ion batteries in the near future.

1. Introduction

In recent years, the increasing usage of fossil fuels in transport vehicles and the refinery industry has produced more toxic gases such as CO, CO_2, and hydrocarbons, which cause severe health problems in human beings, including pneumonia and the blocking of oxygen from the brain, heart, and other vital organs by CO. Importantly, the continued release of CO_2 increases global warming, leading to severe climate change.[1-3] In order to reduce the emissions of greenhouse gases, the exploitation of green-energy sources, including solar and wind energy, instead of fossil fuels is necessary in the present scenario.

Hence, to reduce air pollution, the peoples are focusing on green-energy sources such as solar and wind energy; they can be considered as important alternative energy sources for sustainable economic growth. However, solar and wind energy as well as electric cars require highly efficient energy-storage devices. In recent decades, batteries have been viewed as the most promising energy-storage devices, as they can store electrical energy as electrochemical energy. Batteries are classified into two types: primary and secondary batteries. A primary battery is used in its charged state once it converts its chemical energy into electrical energy; it is then discarded as it is not rechargeable. A secondary battery is electrically rechargeable after discharge. To date, the most investigated secondary batteries have been lead–acid, Ni–Cd, Ni–metal hydride, and Li-ion batteries (LIBs). Among these batteries (Table 1), LIBs have exhibited the best electrochemical performances in terms of long cycle life, low self-discharge, high cell voltage, and no memory effects, and their energy densities are two times and their power densities five times greater than those of current Pd–acid and Ni–Cd batteries.[4] Hence, LIBs are widely used in different electronic devices, including laptops, mobile phones, and other such electronic devices.[5-7]

2. Construction and working principle of LIBs

The LIB is an energy-storage device that converts chemical energy into electrical energy through a controlled, thermodynamically favorable chemical reaction. Generally, such a battery consists of a number of interconnected cells. Each individual cell has a cathode, anode, and electrolyte. Both the cathode and anode are electrically isolated by the electrolyte and a separator in order to avoid a short circuit.

[a] Solid State Ionics and Energy Devices Laboratory, Department of Physics, Bharathiar University, Coimbatore 641 046, Tamil Nadu, India. Email: selvankram@buc.edu.in
[b] Faculty of Applied Chemical Engineering, Chonnam National University, Gwangju 500-757, Korea. Email: leeys@chonnam.ac.kr

View Article Online
DOI: 10.1039/C5RA23503K

The electrolyte is an ionically conductive medium, such as a polymeric/organic electrolyte, that facilitates Li ion transfer between the anode and cathode. Currently, such batteries consist of a layered structure of $LiCoO_2$ and graphite, which are used as the cathode and anode, respectively.

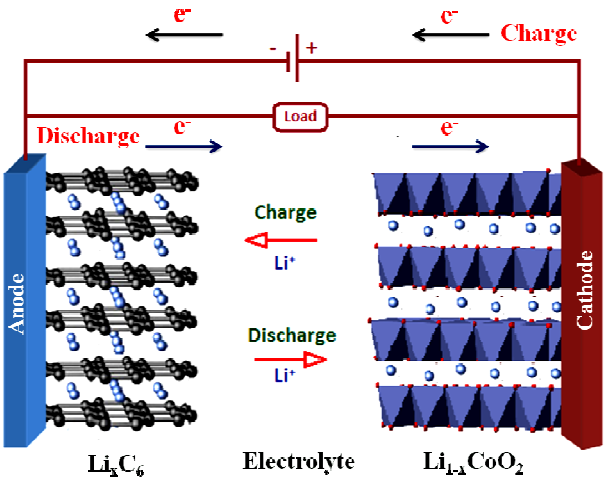

Figure 1. Charge–discharge process of a Li-ion battery (LIB).

In rechargeable batteries, the storage mechanism involves a reversible insertion–extraction of Li ions into and out of the electrode material during the charge–discharge process, based on the rocking-chair concept. While charging (which involves the loss of electrons and Li ions), Li ions are deintercalated from the cathode and intercalated into the anode. In the discharge process, Li ions are deintercalated from the anode and intercalated into the cathode, delivering the energy to an external circuit. This discharge process continues until the potential difference between the two electrodes becomes too small at which point the cell is fully discharged. Figure 1 depicts a schematic diagram of their function, and the reversible-reaction mechanism of LIBs is described as follows,[8,9]

$$\text{Anode:} \quad 6C + xLi^+ + xe^- \leftrightarrow Li_xC_6\,, \qquad (1)$$

$$\text{Cathode:} \quad LiCoO_2 \leftrightarrow Li_{1-x}CoO_2 + xLi^+ + xe^-\,. \qquad (2)$$

Currently, commercially used cathode materials include layered, structured $LiCoO_2$ (140–160 mAh g^{-1}); olivine-type $LiFePO_4$ (140–160 mAh g^{-1}); and spinel-type $LiMn_2O_4$ (100–120 mAh g^{-1}), and their practical energy densities versus a graphite anode are 584, 398, and 424 Wh kg^{-1}, respectively. On the other hand, while using combinations of $Li_4Ti_5O_{12}$ and $LiMn_2O_4$ the obtained energy density is 200 Wh kg^{-1}, which is half of the reported value when using graphite as the anode, since the specific capacity of spinel $Li_4Ti_5O_{12}$ is 175 mAh g^{-1}.[10] The currently used graphite anode has several fascinating properties such as a low working potential versus Li, long cycle life, and low cost. However, its primary drawback is its low reversible capacity, as the diffusion rate of Li is in between 10^{-9} and 10^{-6} cm^2 s^{-1}, resulting in the low power density of this type of battery.[11] Therefore, to further improve the power density of this component, it is mandatory to adopt new strategies and to identify novel materials to replace the graphite anode. Another well-known anode material is Li metal, which possesses a high specific capacity of 3860 mAh g^{-1} and low working potential. However, the working potential of Li metal exists outside the window of the electrolyte, so the transfer of Li ions into the electrode material is achieved through a solid-electrolyte-interphase (SEI) passivation layer that is formed by way of an electrolyte-decomposition process. However, for a fast charge–discharge process, a larger number of Li ions build up on the surface of the Li metal; moreover, changes in the electrode volume break the SEI layer, forming Li plating that leads to dendrite formation. On subsequent cycles, Li dendrites grow across the electrolyte, causing these batteries to short circuit.[8, 12] Therefore, based on safety concerns, Li metal is highly restricted to the application of anodes in LIBs. The most important issue is that commercially used LIBs do not have sufficient energy and power densities for implementation in hybrid-electric and plug-in hybrid-electric vehicles. Generally, the energy and power densities are directly proportional to the cell voltage and specific capacity of a cell (energy density = *VIt* (Wh kg^{-1}). Hence, to achieve high-power- and high-energy-density LIBs, appropriate anode and cathode materials with high specific capacities, cell voltages, and Li-diffusion coefficients are needed. After the pioneering work of Tarascon et al., transition-metal-oxide (*MO*, *M* = Co, Ni, Cu, Fe) nanoparticles have been explored as potential anodes for LIBs. They demonstrated an excellent electrochemical property of 700 mAh g^{-1} with 100% capacity retention after 100 cycles at high charging rates and have suggested that the high electrochemical reactivities of transition-metal oxides might lead to the improved performances of such batteries.[13] The electrochemical reactions of transition-metal oxides are

$$MO + 2Li^+ + 2e^- \leftrightarrow Li_2O + M \ (M = \text{Co, Ni, Fe, and Mn}) \qquad (3)$$

Here, the redox reactions between metal oxides and Li ions are thermodynamically more favorable and involve multiple electron transfers per metal atom, leading to high specific capacities in the range of 500 to 1000 mAh g^{-1}.[14, 15] Even though simple metal oxides have shown high reversible capacities and energy densities, they suffer from low Coulombic efficiencies in the first cycle, unstable SEI-layer formation, large potential hysteresis, and poor capacity retention.[16]
Hence, these drawbacks can be overcome by adopting mixed-metal oxides such as $ZnFe_2O_4$, $NiCo_2O_4$, Co_2GeO_4, and $MnCo_2O_4$ as possible anodes for LIBs due to their high electronic conductivities, fast ionic-transport rates, and easy methods of synthesis. Their different architectures and crystallinity controls may prove these mixed-metal oxides to be good electrochemical-energy-storage materials for LIBs. Recently, Wei et al. demonstrated that complex binary- and ternary-metal oxides possess better electronic conductivities compared to simple metal oxides, and they demonstrated that

View Article Online
DOI: 10.1039/C5RA23503K

$NiCo_2O_4$ has a larger electrochemical activity and an electronic conductivity two orders of magnitude greater than those of simple Ni and Co oxides.[17] These kind of mixed metal oxides has special features like complex chemical composition, interfacial and synersistic effects leads to enhanced electrochemical performance and electronic conductivity.[18, 19] So in order to further emphasize the importance of this type of binary spinel compounds, an attempt is made here to review the electrochemical performance of the mixed metal oxides especially AB_2O_4 and A_2BO_4 structures on the application of Li-ion anode materials.

3. AB_2O_4 structure

The general formula of the spinel structure (AB_2O_4) is $[A^{2+}][B^{3+}{}_2][O_4{}^{2-}]$, where *A* is a divalent cation and *B* is a trivalent cation. This structure consists of a closely packed array of 32 oxygen ions that form 64 tetrahedral cations and 32 octahedral cations in a single unit cell. The spinel structure can be classified into three types: normal, inverse, and mixed spinel based on the cation occupancy.[20, 21] In a normal spinel, the *A* cations preferentially occupy tetrahedral sites, and the *B* cations occupy octahedral sites. Examples of such normal spinels include $MgAl_2O_4$, $ZnFe_2O_4$, and $CdFe_2O_4$. In the inverse-spinel structure, the octahedral sites are occupied by the *A* cations and half of the *B* cations, while the other half of the *B* cations occupy the tetrahedral sites. It is denoted as $[B^{3+}][A^{2+}B^{3+}]O_4$. $CoFe_2O_4$ and $NiFe_2O_4$ are examples of the inverse-spinel structure.[22, 23] In a mixed spinel, both *A* and *B* cations occupy both octahedral and tetrahedral sites, and the molecular formula is $[M^{2+}{}_xFe^{3+}{}_{1-x}][M^{2+}{}_{1-x}Fe^{3+}{}_{1+x}]O_4$. Examples of mixed spinels include $NiCo_2O_4$, $MnCo_2O_4$, and $CoMn_2O_4$.

There are three different possible charge-storage mechanisms involved in anode materials: intercalation–deintercalation, alloying–de-alloying, and conversion reactions.[24-26]

1. Normally, intercalation–deintercalation mechanisms occur in carbon-based materials such as carbon nanotubes (CNTs), graphene, porous carbon, TiO_2, and $Li_4Ti_5O_{12}$.

$$MO_z + xLi^+ + xe^- \leftrightarrow Li_xMO_z \text{ (M = Ti and W)} \quad (4)$$

2. Similarly, the alloying–de-alloying mechanism occurs with Si, Ge, Sn, Bi, SnO_2, SiO_2, GeO_2, and so on.

$$MO_x + 2xLi^+ + 2xe^- \rightarrow M + xLi_2O \quad (5)$$

$$M + xLi^+ + xe^- \leftrightarrow Li_xM \text{ (M = Si, Sn, Sb, and Ge)} \quad (6)$$

In the case of pure Zn, Ge, Sn and Si electrodes, the charges are stored through alloying/de-alloying mechanism by forming Li_xZn, Li_xGe, Li_xSn and Li_xSi, respectively, according to eqn (6). On the other hand, the metal oxides including ZnO, GeO_2 and SnO_2 based electrodes involving both conversion and alloying/de-alloying mechanism, according to eqn (5 and 6). This different charge storage mechanism mainly arises from the oxygen molecules.

3. The conversion-reaction mechanism is applicable to transition-metal oxides such as MnO_2, Mn_2O_3, NiO, Fe_2O_3, Fe_3O_4, Co_3O_4, CoO, and CuO.

$$M_zO_x + 2xLi^+ + 2xe^- \leftrightarrow zM + xLi_2O \text{ (M = Co, Ni and Fe)} \quad (7)$$

The pure Co, Fe, Mn and Ni elements are electrochemically inactive. But, it involved in the conversion reaction, while in the form of metal oxides. So the main contribution arises from the decomposition and reformation of Li_2O amorphous matrix according to eqn (7).

Generally, the mixed metal oxides store the lithium ions through both conversion reaction as well as alloying/de-alloying mechanism.[27-29] In $M_2M'O_4$ (M= Co, Fe, Mn and Ni; M' = Sn, Ge and Si) system, during first discharging process the active material disintegrated into its constituent elements (M and M') followed by the formation of Li_2O amorphous matrix and electrolyte decomposition at 0.6 to 0.7 V vs. Li/Li^+.[30] Subsequently, the M' reacts with lithium to form Li_xM' (Li-alloying formation) at 0.1 to 0.3 V vs. Li/Li^+ [3]. During charging process, de-alloying reaction takes place at 0.5 to 0.8 V vs. Li/Li^+, and yielded individual metals (M and M'). Subsequently, this metal particles act as catalyst to decompose the Li_2O amorphous matrix and formed a corresponding oxides (MO_x and $M'O_x$), according to conversion reaction mechanism.[13] In the case of $MM_2'O_4$ (M = Ni, Mn, Co and Fe; M'=Ni, Mn, Co and Fe), the elements M and M' are involved in conversion reaction mechanism. During the first discharging process, the crystal structure destructed into individual metal particles accompanying with the formation of Li_2O matrix. As produced metal particles facilitate the electrochemical activity by means of formation/decomposition of Li_2O that give the way for conversion reaction mechanism.[31]

In the following sections, the main significance and electrochemical performances of these different types of structured spinel materials such as ferrites (AFe_2O_4), cobaltites (ACo_2O_4), manganites (AMn_2O_4) (where *A* = Mg, Zn, Cu, Mn, Ni, and Co), and A_2BO_4 (where *A* = Co, Zn, Mn, and *B* = Sn, Ge, and Si)-structured materials are discussed.

3.1. AFe_2O_4 (*A* = Mg, Zn, Cu, Mn, Ni, and Co)

Generally, AFe_2O_4-based spinel ferrites possess good electrical and magneto-optical properties, according to the *A*- and *B*-site cation distribution, and they have been widely investigated for applications in different fields, including the electronics industry, magnetic recording, magnetic-resonance imaging, and ferrofluids.[32-34] Ferrite-based materials are abundant, cheap, and environmentally friendly. The spinel-ferrite MFe_2O_4 (*M* = Mg, Zn, Cu, Mn, Ni, and Co)-based materials exhibit significant discharge capacities of 1000 mAh g^{-1}, which is two

View Article Online
DOI: 10.1039/C5RA23503K

to three times greater than that of commercially used graphite anodes.[35]

3.1.1. $MgFe_2O_4$

$MgFe_2O_4$ has a mixed-spinel structure, and its formula is $[Mg_{1-x}Fe_x]^{IV}[Mg_xFe_{2-x}]^{VI}O_4$, where *x* is the inversion parameter and denotes the fraction of *B* cations in the tetrahedral sites. It consists of a face-centered close-packed oxygen sublattice in which the tetrahedral sites are filled by Mg^{2+} ions and a fraction of the Fe^{3+} ions and the octahedral sites are filled by the Fe^{3+} ions and a fraction of the Mg^{2+} ions.[36] Pan et al. prepared $MgFe_2O_4$ nanoparticles via a sol–gel method and reported a discharge capacity of 474 mAh g^{-1} at 90 mA g^{-1} over 50 cycles. Sadly, it delivered only 293 mAh g^{-1} after 50 cycles when the current density was increased to 900 mA g^{-1}.[37] On the other hand, Gong et al. prepared carbon-coated $MgFe_2O_4$ nanoparticles (Figure 2(a, b)) for which the thickness of each carbon layer was 4 nm. According to the electrochemical reaction (Eqs. 8 and 9), MgO does not react with Li, preventing the aggregation of Fe oxides during the charge–discharge process and also acting as a buffer matrix during the insertion–deinsertion process,[38]

$$Li_{0.56}MgFe_2O_4 + 5.44Li^+ + 5.44e^- \rightarrow MgO + 2Fe + 3Li_2O\ , \quad (8)$$

$$3Fe + 4Li_2O \rightarrow Fe_3O_4 + 8Li^+ + 8e^-\ . \quad (9)$$

The carbon-coated $MgFe_2O_4$ electrode demonstrated a high specific capacity of 466 mAh g^{-1} at a high current density of 1600 mA g^{-1} and a greater rate capability than carbon-coated Fe_3O_4 (Figure 2(c)). This high rate capability as well as its good cycling stability was achieved through its smaller grain size, MgO matrix, and carbon coating. These factors facilitated a short diffusion-path length for the Li^+ ions, preventing particle agglomeration and enhancing the electrical conductivity. The carbon coating not only enhanced the electrical conductivity of the material but also accommodated the volume expansion during the charge–discharge process. It is well known that utilizing graphene composites is an important strategy to improve the electrical conductivity and to prevent volume expansion during the insertion–deinsertion process, and it can provide a large number of accessible active sites for Li^+ ion insertion and a short diffusion-path length for both Li^+ ions and electrons due to the synergistic effects between the active material and graphene. The prepared $MgFe_2O_4$–graphene-nanocomposite electrode showed a high reversible discharge capacity of 764.4 mAh g^{-1} at 0.04*C* over 60 cycles and retained a capacity of 219.9 mAh g^{-1} at a high current rate of 4.2*C*.[39] The carbon-coated and graphene-composite $MgFe_2O_4$ particles demonstrated better electrochemical performances than did the regular $MgFe_2O_4$ nanoparticles.

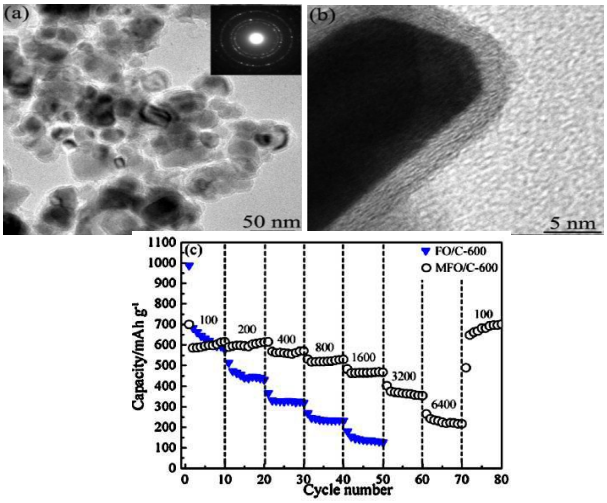

Figure 2. (a-c) Carbon-coated $MgFe_2O_4$ nanoparticles and their rate-capability curves. (Reprinted with permission from ref. 38. Copyright 2013 Elsevier.)

3.1.2. $ZnFe_2O_4$

$ZnFe_2O_4$ has a normal-spinel structure in which the Zn^{2+} cations occupy the tetrahedral sites and the Fe^{3+} cations occupy the octahedral sites.[40, 41] $ZnFe_2O_4$ is considered to be a good candidate for anode materials, given its high specific capacity around 1000 mAh g^{-1}. The charge-storage mechanism of $ZnFe_2O_4$ results primarily from the alloying–de-alloying- and conversion-reaction mechanisms. Sharma and coworkers synthesized $ZnFe_2O_4$ using a combustion method, examined the charge-storage properties, and explained the charge-storage mechanism through TEM images and selected area electron diffraction (SAED) patterns, given the following reactions,[42]

$$ZnFe_2O_4 + 0.2Li^+ + 0.2e^- \rightarrow Li_{0.2}ZnFe_2O_4 \quad (10)$$

$$Li_{0.2}ZnFe_2O_4 + 7.8Li^+ + 7.8e^- \rightarrow Zn + 2Fe + 4Li_2O \quad (11)$$

$$Zn + Li^+ + e^- \leftrightarrow LiZn \quad (12)$$

$$Zn + Li_2O \leftrightarrow ZnO + 2Li^+ + 2e^- \quad (13)$$

$$2Fe + 2Li_2O \leftrightarrow 2FeO + 4Li^+ + 4e^- \quad (14)$$

During the first discharge process, i.e., from OCV to 0.8 V, 0.2 mol of Li ions intercalated into the crystal structure, according to Eq. 10. Below the potential of 0.8 V, intercalation of Li ions led to the deterioration of the crystal structure of $ZnFe_2O_4$ into LiZn, ZnO, FeO, and Li_2O matrices in which Li_2O was involved in the reversible reaction. Generally, the first cycle was considered to be an irreversible reaction, and it possessed a high irreversible capacity due to the formation of the SEI layer, the side reaction of the electrolyte with the active material layer, and the amorphous-Li_2O formation. In the second cycle, the $ZnFe_2O_4$ nanoparticles possessed a discharge capacity of 800 mAh g^{-1} at 60 mA g^{-1}, which decreased to 615 mAh g^{-1} after 50 cycles due to the volume

View Article Online
DOI: 10.1039/C5RA23503K

expansion of the active material, which in turn was due to the alloying–de-alloying- and conversion-reaction mechanisms. To overcome this problem, Teh and coworkers[43] prepared one-dimensional (1D) $ZnFe_2O_4$ nanofibers that exhibited a high specific capacity of 920 mAh g^{-1} in the first cycle at 60 mA g^{-1} and 733 mAh g^{-1} after 30 cycles. Consequently, they had a capacity of 400 mAh g^{-1} at 800 mA g^{-1}, a value that was high compared with that of the commercially used graphite anode. It has been reported that this enhanced capacity arises mainly from this morphology of $ZnFe_2O_4$ as the $ZnFe_2O_4$ nanofibers are well connected with nanoparticles and they act as electronic wiring during the charge–discharge process.[43] Hence, tuning the morphology and size of an electrode material effectively enhances its specific capacity and rate capability. Various researchers have proposed further increasing the rate capability of the $ZnFe_2O_4$ material with different carbonaceous-material composites, morphological features, and binder effects.[44-54] Mesoporous, $ZnFe_2O_4$ carbon-composite microspheres demonstrated good electrochemical performance as well as a high reversible capacity of 1100 mAh g^{-1} at a current density of 0.05 A g^{-1} over 100 cycles. The carbon composite not only enhanced their specific capacity but also facilitated a superior rate capability that provided a discharge capacity of 600 mAh g^{-1} at a high current density of 1 A g^{-1}. Recently, Yao and coworkers prepared a mesoporous $ZnFe_2O_4$–graphene composite, which exhibited excellent electrochemical performance due to the synergistic effects between the large surface areas of the $ZnFe_2O_4$ nanoparticles and the excellently flexible and highly electronically conductive graphene. The mesoporous $ZnFe_2O_4$–graphene composite had a high specific capacity of 870 mAh g^{-1} at 1 A g^{-1} after 100 cycles and demonstrated a good rate capability. Nonetheless, it retained a specific capacity of 713 mAh g^{-1} at 2 A g^{-1}, indicating the ultrafast charging capability and good cycling stability of this mesoporous $ZnFe_2O_4$–graphene composite.[54] Table 2 lists the overall electrochemical performances of $ZnFe_2O_4$ and its composites, synthesized by various techniques.

Another method to improve specific capacity is by forming mesoporous microspheres, since they form from well-interconnected nanoparticles. Therefore, they increase the interfacial surface reactions with Li and shorten the diffusion path for Li ions and electrons, leading to high specific capacities. The interconnected nanoparticles create these mesopores in between neighboring particles, thereby accommodating the volume expansion during the charge–discharge process.[52] Furthermore, the interconnected nanoparticles embedded in the carbon matrix also enhanced the intrinsic electrical conductivity and thus speeded the transport of Li^+ ions and electrons. Therefore, this type of mesoporous-carbon-composite structure facilitates high reversible specific capacities, good cycling stabilities, and good rate capabilities of electrodes.

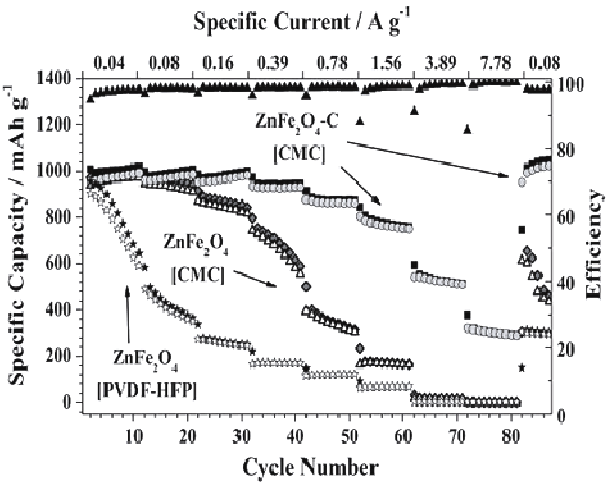

Figure 3. Rate capabilities of carbon-coated $ZnFe_2O_4$ nanoparticles using different binders (circles: $ZnFe_2O_4$–C, triangles: $ZnFe_2O_4$–CMC, and stars: $ZnFe_2O_4$–PVDF-HFP). (Reprinted with permission from ref. 53. Copyright 2013, Wiley-VCH Verlag GmbH & Co. KGaA.)

In addition, other than carbon composites and mesoporous structures, a binder can also effectively alleviate the volume-expansion problem. Bresser et al. used sodium carboxymethyl cellulose (NaCMC) as a binder for carbon-coated $ZnFe_2O_4$ nanoparticles, and Figure 3 depicts its corresponding cycling-stability curve.[53] This binder promoted superior electrochemical performance as a result of the stable reversible capacity (1300 mAh g^{-1}) at 0.04 A g^{-1} over 100 cycles and 525 mAh g^{-1} at a high current density of 3.89 A g^{-1}. The main advantages of the CMC binder are that it is nontoxic, eco-friendly, and water soluble; therefore, it provides better contact between the active material and the current collector and modifies the SEI formation due to the continuous reaction of CMC with organic electrolytes, enhancing the cycling stability and already high rate capability.

3.1.3. $CuFe_2O_4$

$CuFe_2O_4$ possesses an inverse-spinel structure, and it has been widely investigated as an anode material due to its low cost, high abundance, environmental friendliness, and high theoretical specific capacity of 895 mAh g^{-1}. A number of factors limit the implementation of $CuFe_2O_4$ as an anode material, including its low inherent electronic conductivity and volume expansion during lithium insertion and extraction process. To overcome this problem down the particle size from bulk to nanolevel and making composite with the carbonaceous material is required.[55] The spinel-$CuFe_2O_4$ structure undergoes a conversion reaction during the charge–discharge process as follows,[56-59]

$$CuFe_2O_4 + 8Li^+ + 8e^- \rightarrow 4Li_2O + Cu + 2Fe \quad (15)$$

$$Cu + 2Fe + 4Li_2O \leftrightarrow CuO + Fe_2O_3 + 8Li^+ + 8e^- \quad (16)$$

View Article Online
DOI: 10.1039/C5RA23503K

Ding et al. prepared the $CuFe_2O_4$ nanoparticles which possess a high specific capacity of 840 mAh g^{-1} in the second cycle; further increasing the number of cycles decreases the capacity to 551 mAh g^{-1}.[55] Normally, the nanoparticles have high surface energies, which often result in self-aggregation and lead to less surface area overall as well as the easy diffusion of the electrolyte ions, in turn leading to severe capacity fading. Significantly, Jin et al. reported the preparation of hollow $CuFe_2O_4$@C nanospheres and $CuFe_2O_4$@C nanoparticles via a polymer-templated hydrothermal method, followed by calcination to create the carbon shells. Among these compounds, hollow, carbon-coated $CuFe_2O_4$ nanospheres demonstrated a good cyclic performance of 550 mAh g^{-1} at 100 mA g^{-1} over 70 cycles, whereas hollow $CuFe_2O_4$ only showed 120 mAh g^{-1} and $CuFe_2O_4$@C nanoparticles only showed 300 mAh g^{-1}. The carbon layer and hollow space influenced the electrochemical performance of hollow $CuFe_2O_4$@C, effectively accommodating the volumetric changes during the cycling process, mitigating the agglomeration between the particles, and facilitating the electron transport that enhanced the specific capacity and good rate performance of the electrode material.[57]

3.1.4. $MnFe_2O_4$

The spinel manganese ferrite is a promising candidate for several applications, including semiconductors, biosensors, photocatalysts, supercapacitors, and medical applications.[55-59] However, only a sparse number of reports are available concerning $MnFe_2O_4$ with regards to its application to anode materials in LIBs.[65, 66] $MnFe_2O_4$ stores Li ions through a conversion reaction ($MnFe_2O_4 + 8Li^+ + 8e^- \leftrightarrow Mn + 2Fe + 4Li_2O$), and it exhibits a high theoretical specific capacity of 928 mAh g^{-1}. Zhang et al. synthesized mesoporous manganese ferrite microspheres using a solvothermal method and examined their electrochemical performance versus Li metal. These microspheres showed a high reversible discharge capacity of 712 mAh g^{-1} at a rate of 0.2*C* over 50 cycles. Only feeble capacity fading was observed over each cycle, and they retained a capacity of 552 mAh g^{-1} even at a high current density at a rate of 0.8*C*.[65] This reported capacity fading was an acceptable limit and was achieved without fabricating any sort of composite with carbon, CNTs, or graphene. As explained above, the porous nature of these microspheres could accommodate the volume changes during the conversion reaction. The appropriate grain size with crystallinity might improve the surface area of the active material, and the electronic conductivity of the electrode material thus could lead to both an improved specific capacity and cycling stability.[66-68] Furthermore, Xiao et al. prepared $MnFe_2O_4$–graphene nanocomposites via an ultrasonication process to improve their electrochemical properties.[69] A graphene composite has several advantages such as its enhanced inherent conductivity and high surface area (2600 m^2 g^{-1}), and it stores Li^+ ions through an insertion–de-insertion process, thereby demonstrating its high theoretical specific capacity of 744 mAh g^{-1} at the same time that it can accommodate volume expansion.[70] The $MnFe_2O_4$–graphene composite possessed a high specific capacity of 1017 mAh g^{-1} at 100 mA g^{-1} over 90 cycles and 960 mAh g^{-1} at 1000 mA g^{-1}. It also showed an excellent rate capability.[69]

3.1.5. $NiFe_2O_4$

$NiFe_2O_4$ is also considered a promising anode material for LIBs, since it can accommodate 8 mol of Li per formula unit; therefore, it has a high theoretical specific capacity of 914 mAh g^{-1}. It stores Li^+ ions through an electrochemical-conversion reaction as follows,[71-74]

$$NiFe_2O_4 + 8Li^+ + 8e^- \rightarrow Ni + 2Fe + 4Li_2O \quad (17)$$

$$Ni + Li_2O \leftrightarrow NiO + 2Li^+ + 2e^- \quad (18)$$

$$2Fe + 3Li_2O \leftrightarrow Fe_2O_3 + 6\,Li^+ + 6e^- \quad (19)$$

However, there are numerous difficulties in implementing $NiFe_2O_4$ as an anode material because of the low diffusion of Li ions in the bulk material, low conductivity, and large volume expansion during the charge–discharge process.[71-73] Several reports have proposed solutions to overcome this issue so as to synthesize nanosized particles with porous structures and conducting carbon networks to improve the electrochemical performance of $NiFe_2O_4$.[74-76] Macroporous $NiFe_2O_4$ particles were prepared via a sol–gel method using a citrate precursor. The sample, calcined at 800 °C, showed better cycling stability and a better rate capability due to its smaller particle sizes with larger pore sizes, as compared to a sample calcined at 1000 °C, and it maintained a capacity of 600 mAh g^{-1} after 80 cycles at a rate of 1*C*.[73] Morphological features also play an important role in enhancing the electrochemical performance. Recently, $NiFe_2O_4$ nanofibers were synthesized via an electrospinning technique, and their electrochemical performance was compared with that of $NiFe_2O_4$ nanoparticles.[74] The cycling-stability curve indicated that the $NiFe_2O_4$ nanofibers exhibited a superior electrochemical performance as compared to the nanoparticles. The $NiFe_2O_4$ nanofibers showed only feeble capacity fading in the initial 15 cycles due to the structural rearrangement of the active material, as they were well connected with conductive carbon and had stable SEI formation. After 15 cycles, the capacity stabilized at 870 mAh g^{-1} at 100 mAh g^{-1} for another 40 cycles. In the subsequent cycles, the capacity increased steeply to 1000 mAh g^{-1} over 100 cycles. This reported specific capacity was greater than the theoretical specific capacity; it was attained through a kinetically activated electrolyte degradation.[77, 78] Imperatively, binders also effectively contribute to the electrochemical performance. Many authors have reported using different binders such as polyvinylidene fluoride (PVDF), polyacrylic acid (PAA), CMC, and sodium alginate for electrode preparation.[79-82] Ramesh and coworkers reported that they synthesized nanocrystalline $NiFe_2O_4$ via a sol–gel-combustion route and examined its electrochemical performances using PVDF and sodium alginate as binders. The cycling-stability curve clearly illustrated the severe capacity fading of the $NiFe_2O_4$ nanoparticles at a rate of

View Article Online
DOI: 10.1039/C5RA23503K

0.1 *C*, which indicated the inadequate interfacial stability of the PVDF binder.[82] However, in the case of the $NiFe_2O_4$ nanoparticles with sodium alginate, the nanoparticles showed a stable discharge capacity of 880 mAh g^{-1} over 30 cycles at a current density of 92 mA g^{-1} without any degradation of the discharge capacity. Further studies of the rate performance of this electrode material were carried out using a sodium alginate binder at different current densities. The discharge-capacity values decreased to 620, 504, 420, and 380 mAh g^{-1} when the current density was increased to 1*C*, 2*C*, 5*C*, 10*C*, and 20*C*, respectively. The $NiFe_2O_4$ nanoparticles with sodium alginate had a discharge capacity of 380 mAh g^{-1} at a high current density of 18,300 mA g^{-1} at a rate of 20*C*, as shown in Figure 4, and they demonstrated a good rate capability as compared with the ternary composite.[79] The sodium alginate binder effectively improved the cycle life and exhibits good rate capability, compared to commercially used PVDF, as the PVDF could not accommodate any volume strain during the cycling process. On the other hand, sodium alginate contains carboxylic groups evenly distributed in the polymer chain that improve the transport of Li ions and increase the stablility of the SEI-layer formation. It also possesses polar molecules that improve the interfacial interaction of the polymer binder and facilitate the self-healing process during the charge–discharge process. Furthermore, it provided strong adhesion between the electrode layer and the Cu substrate.[81, 83, 84] The $NiFe_2O_4$ nanoparticles with sodium alginate binder showed superior electrochemical performance, as compared to previously reported $NiFe_2O_4$–graphene heteroarchitectures.[85]

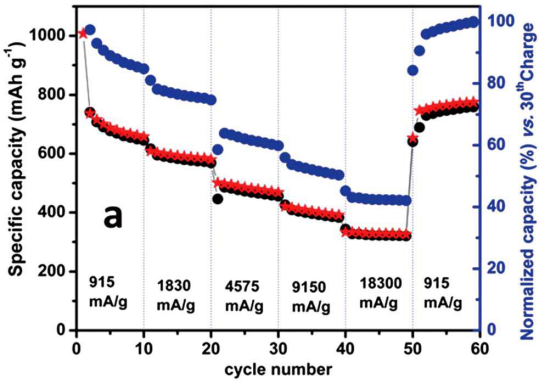

Figure 4. Rate capabilities of the $NiFe_2O_4$ nanoparticles with sodium alginate binder at different current densities. (Reproduced from Ref. 82. Copyright 2013, with permission from the royal society of chemistry.)

3.1.6. $CoFe_2O_4$

Cobalt ferrite is a thoroughly investigated anode material used for LIBs due its low cost, environmental friendliness, and high chemical stability. It also stores Li ions through a conversation reaction similar to that of $NiFe_2O_4$, and it possesses a high theoretical specific capacity of 914 mAh g^{-1}.[86-88] However, it has severe drawbacks such as a large volume change that induces the pulverization and aggregation of the active material and low conductivity that leads to poor cycling stability and a low rate capability of the $CoFe_2O_4$ particles.[89-91] To achieve better performance, $CoFe_2O_4$ nanoparticles have been synthesized with different morphologies, including hollow nanospheres, mesoporous nanospheres, and nanorods, and as composites with different conducting matrices.[46, 92-95] In particular, Xiong et al. prepared different morphologies of $CoFe_2O_4$, such as irregular particles, microspheres, and flower-like microspheres (Figure 5a), via a hydrothermal method using various concentrations of ascorbic acid. Among these morphologies, the flower-like microspheres had the largest surface areas of 51.0 m^2 g^{-1} compared to the regular microsphere and the irregular particles. Similarly, the flower-like microspheres (Fig. 5(b)) had a high reversible specific capacity of 790 mAh g^{-1} at a current density of 200 mA g^{-1}, and even when the current density increased to 1000 mA g^{-1}, they still maintained their high discharge capacity of 744 mAh g^{-1}.[96]
The high reversible capacity and rate capability attained through good electronic conductive wetting of the active materials thus facilitated a rapid charge-transfer process during the insertion–deinsertion process.[97] Recently, Zhang et al. reported the superior electrochemical performance of mesoporous $CoFe_2O_4$ nanospheres with cross-linked CNTs.[93] The CNT-weight ratios varied between 10, 20, and 30 wt%. Among these values, the $CoFe_2O_4$ with 20 wt% CNTs is shown in Fig. 5c which possessed the highest specific capacity of 1046 mAh g^{-1} after 100 cycles at a current density of 100 mA g^{-1} with a good cycling stability and rate capability (Fig. 5d), as compared to the $CoFe_2O_4$–graphene composite.[93, 95] The SEM results of after charge-discharge cycles indicated that the formation of a small amount of SEI film on the active surfaces led to a fast conversion reaction and that the CNTs accommodated the volume changes during the charge–discharge process.[98] On the other hand, Kumar et al. reported that porous $CoFe_2O_4$–rGO with an alginate binder showed an excellent rate performance Fig. 5e) compared to both CNTs and graphene composite.[88] Therefore, a novel binder and a conductive matrix both play essential roles in improving the cycling stability as well as the rate capability of an electrode material. As such, it can be concluded that $MgFe_2O_4$, $CoFe_2O_4$, and $NiFe_2O_4$ are not suitable anode materials. After the first lithiation process, $MgFe_2O_4$ converts into MgO, Fe, and a Li_2O matrix in which MgO does not participate in the electrochemical reaction, leading to a low specific capacity. So too, while $CoFe_2O_4$ has been considered as an important anode material, it is costly, and its high working potential (2.1 V vs Li/Li^+) reduces the cell voltage. Finally, $NiFe_2O_4$ is both highly expensive and toxic.[99] Therefore, these inherent characteristics restrict the use of $MgFe_2O_4$, $CoFe_2O_4$, and $NiFe_2O_4$ in potential applications requiring high-energy-density LIBs. $ZnFe_2O_4$ and $MnFe_2O_4$ are environmentally friendly and have low working potentials, and their high specific capacities could pave the way for the construction of efficient high-energy-density batteries.

View Article Online
DOI: 10.1039/C5RA23503K

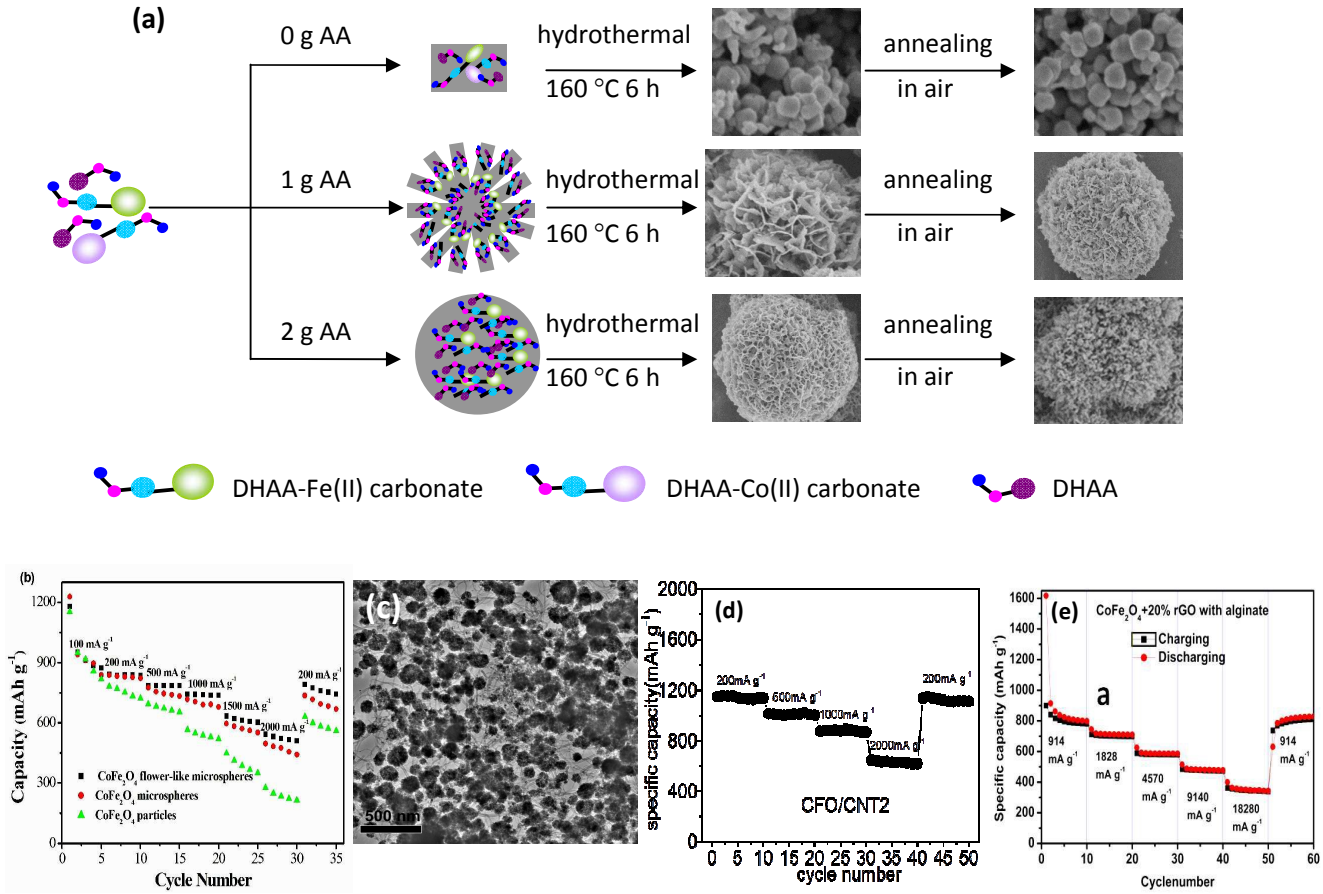

Figure 5. (a, b) Schematic diagram of the reaction producing various morphologies of $CoFe_2O_4$ particles and rate capability curve, (Reprinted with permission from ref. 96. Copyright 2014 Elsevier.) (c, d) TEM image of $CoFe_2O_4$ with 20 wt% CNT and its rate capability curve, (Reproduced from Ref. 93. Copyright 2013, with permission from the royal society of chemistry.) and (e) Rate capability curve of $CoFe_2O_4$ + 20 wt% graphene with a sodium alginate binder. (Reproduced from Ref. 88. Copyright 2014, with permission from the Centre National de la Recherche Scientifique (CNRS) and the Royal Society of Chemistry.)

3.2. AMn_2O_4 (*A* = Co, Ni, and Zn)

It is well known that Mn is environmentally benign, highly safe, low in cost, and abundant in nature compared to Co. With respect to anode materials, Mn-based oxides have lower operating voltages (~1.5 V), reduce the source of Co in mixed-transition-metal oxides, and correspondingly increase the energy density as well as the output cell voltage of such anodes. Therefore, investigating the peculiar properties of manganite-based mixed-transition-metal oxides [AMn_2O_4 (*A* = Co, Ni, Zn)] for applications to LIBs is very necessary.[100, 101] $CoMn_2O_4$ spinels have been synthesized with different morphologies, including hierarchical microspheres, double-shelled hollow microcubes, CNF@$CoMn_2O_4$ nanocables, nanorods, and nanofibers, in attempts to achieve stable capacities and good rate capabilities for electrode materials.[102, 104-106] Significantly, Hu et al. prepared hierarchical $CoMn_2O_4$ microspheres, assembled with porous nanosheets, which possessed large pores between the neighbouring nanosheets [Figure 6(a)], via a solvothermal method.[97] These microspheres exhibited a slight decrease of their specific capacity only a few cycles after that capacity reached 894 mAh g^{-1}, a value that was close to their theoretical specific capacity of 920 mAh g^{-1}, over 60 cycles with excellent cycling stability [Figure 6(b)]. It has been reported that generally at low current densities, the electrolyte ions easily penetrated into the inner parts of the active material and utilized all the active sites, and over subsequent cycles, the observed increase in capacity resulted from the full conversion reaction of the active material. These hierarchical microspheres also had a high specific capacity of 559 mAh g^{-1} at a rate of 4*C* [Figure 6(c)], ensuring a good rate capability of the active material. It has been concluded that porous $CoMn_2O_4$ hierarchical microspheres provided a short diffusion length for both Li ions and electron transport within the electrolyte–electrode interface and accommodated the volume expansion and easy diffusion of the electrolyte into open pores, while the well-interconnected nanosheets enhanced the energy and power densities. Lou et al. recently synthesized carbon-nanofiber–metal-oxide coaxial nanocables using two steps, a polyol method and subsequent thermal annealing. The morphology of the CNF@$CoMn_2O_4$ nanocables and their cycling stability are shown in Figures 6(d)–6(f). The cycling-stability curve of these nanocables provided a high specific capacity of 870 mAh g^{-1} at a

View Article Online
DOI: 10.1039/C5RA23503K

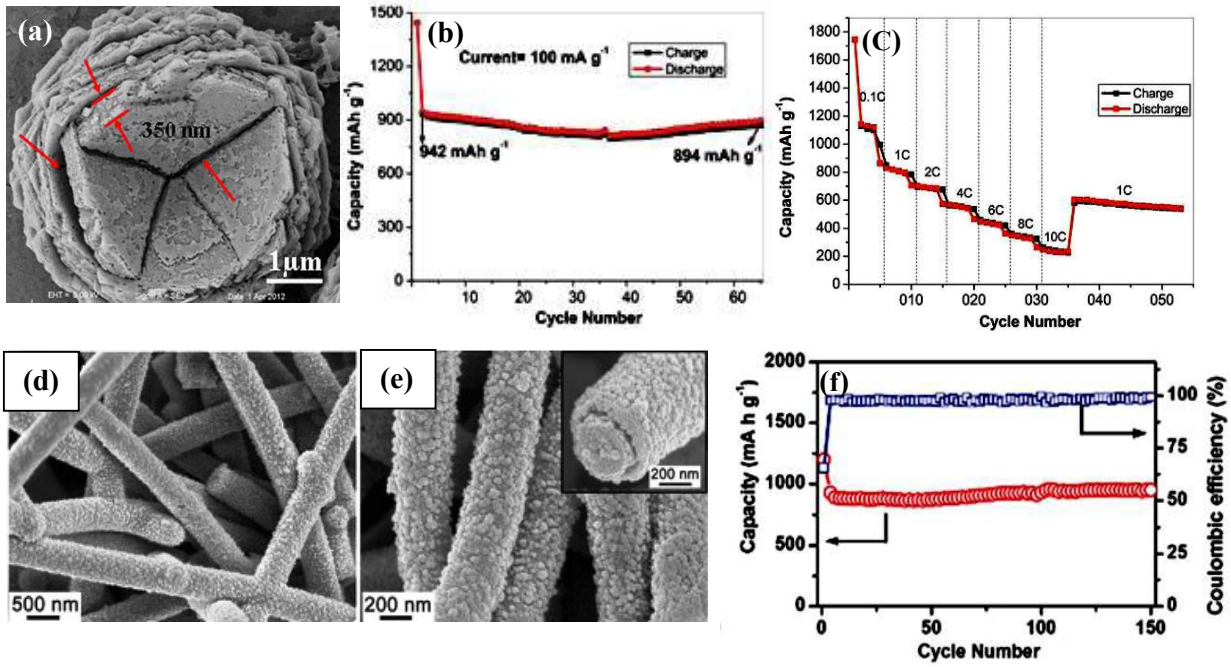

Figure 6. (a)–(c) Hierarchical microsphere of $CoMn_2O_4$ and its cycling stability and rate-capability curve, respectively. (Reprinted with permission from ref. 97. Copyright 2012, Nature Publishing Group.) (d)–(f) HRSEM images of CNF@$CoMn_2O_4$ nanocables and their cycling-stability curve, respectively. (Reproduced from Ref. 104. Copyright 2014, with permission from the royal society of chemistry.)

current density of 200 mA g^{-1} over 150 cycles, and they maintained a capacity of 650 mAh g^{-1} even at a high current density of 1000 mA g^{-1}. These results confirmed the superior electrochemical performance of CNF@$CoMn_2O_4$, as the outer shells of the $CoMn_2O_4$ cables were strongly anchored to the carbon nanofibers and the inner cores of the CNFs could accommodate the volume change during the Li insertion–extraction process, providing good electrical conductivity and thus leading to a high capacity, long cycle life, and good rate performance.[99]

$NiMn_2O_4$ has also been considered as an attractive anode material for LIBs. Lee's group recently synthesized hierarchical tremella-like $NiMn_2O_4$/C nanostructures through a simple solvothermal method followed by a calcination process.[102] The tremella-like nanostructures demonstrated a discharge capacity of 2130 mAh g^{-1} after 350 cycles at a current density of 1000 mA g^{-1}, a value that is greater than the theoretical specific capacity of $NiMn_2O_4$ (~922 mAh g^{-1}), and they retained a high discharge capacity of 1773 mAh g^{-1} at 4000 mA g^{-1} after 1500 cycles. This high discharge capacity arose due to an interfacial-storage mechanism, which originated from the reversible formation–dissolution of an organic polymeric gel-like layer via electrolyte decomposition that induces the extra capacity in the electrode material by way of pseudocapacitive behavior. The small amount of carbon facilitated this high rate capability, prevented the destruction of the hierarchical structure, and provided for continuous electron transport.[107, 108]

Compared with $CoMn_2O_4$ and $NiMn_2O_4$, $ZnMn_2O_4$ has several attractive features, including the fact that it is environmentally friendly; Zn and Mn are also more abundant and lower in cost compared to Ni and Co. In terms of applications, Zn (1.2 V) and Mn (1.5 V) exhibit lower oxidation potentials than does Co (2.2–2.4 V). The low oxidation potentials of Zn and Mn eventually increase the cell voltage and energy density of a battery. $ZnMn_2O_4$ has a high theoretical capacity of 1008 mAh g^{-1} in the first lithiation process due to the conversion and alloying-reaction mechanisms,[110-113]

$$ZnMn_2O_4 + 9Li^+ + 9e^- \rightarrow ZnLi + 2Mn + 4Li_2O \quad (20)$$

$$ZnLi + 2Mn + 3Li_2O \leftrightarrow ZnO + 2MnO + 7Li^+ + 7e^- \quad (21)$$

However, in the second reversible reaction, only 7 mol of Li is contributed to the energy storage, and therefore, this compound has a specific capacity of 784 mAh g^{-1}. As such, its capacity is twice as large as that of a conventional graphite anode. Zhang et al. synthesized nanocrystalline $ZnMn_2O_4$ (Figure 7(a) using a polymer-pyrolysis route and reported the first investigation of this compound for use as an anode material for LIBs.[110] In the initial ten cycles, the discharge capacity decreased up to 20% due to the formation of an SEI film on the surface of the active material is shown in figure 7(b).

View Article Online
DOI: 10.1039/C5RA23503K

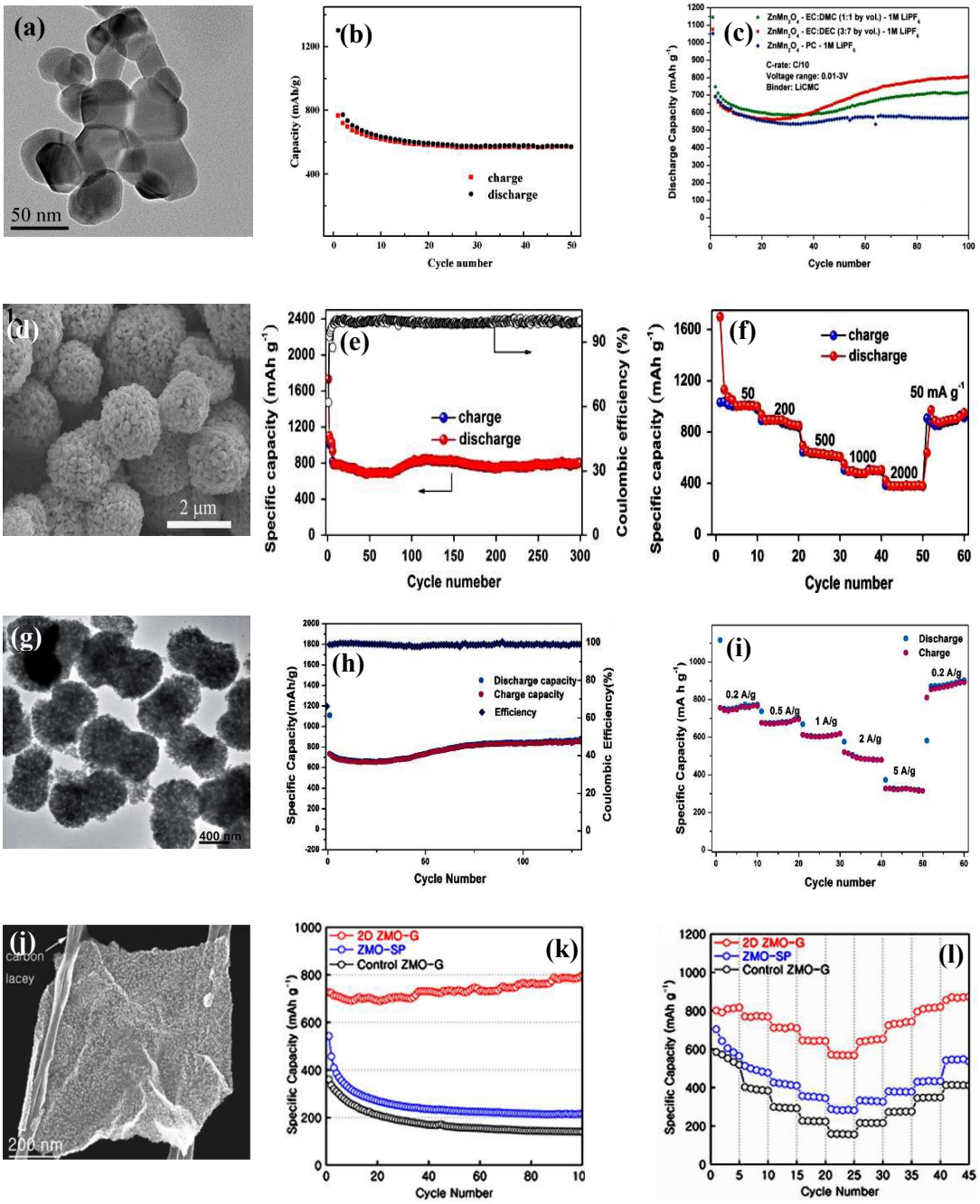

Figure 7. (a)–(b) $ZnMn_2O_4$ nanoparticles synthesized via a coprecipitation method, (Reprinted with permission from ref. 110. Copyright 2008 Elsevier.) (c) cycling stability of $ZnMn_2O_4$ calcined at 800 °C, and its cycling-stability curves with different binders, respectively. (Reproduced from Ref. 99. Copyright 2011, with permission from the royal society of chemistry.) (d)–(f) FESEM image of $ZnMn_2O_4$ microspheres, their cycling-stability curve, and different current densities, respectively. (Reprinted with permission from ref. 116. Copyright 2014 Elsevier) (g)–(i) TEM image of twin microspheres of $ZnMn_2O_4$, their cycling stability, and their rate-capability curves, respectively. (Reproduced from Ref. 117. Copyright 2014, with permission from the royal society of chemistry.) (j)–(l) TEM image of $ZnMn_2O_4$–graphene, its cycling-stability curves, and different current densities, respectively. (Reprinted with permission from ref. 119. Copyright 2014, American Chemical Society)

However, after ten cycles, only 0.20% capacity fading was observed, and a stable capacity of 569 mAh g^{-1} was maintained after 50 cycles. To implement $ZnMn_2O_4$ in LIB applications, its electrochemical performance was enhanced with different morphologies and sizes, using various synthetic techniques that are listed in Table 3. Courtel et al. synthesized $ZnMn_2O_4$ particles via a simple coprecipitation route and optimized their electrochemical performance by varying the different reaction conditions such as the sintering temperature, binder, and electrolyte.[99] Among the sintered (400, 600, 800, and 1000 °C)

View Article Online
DOI: 10.1039/C5RA23503K

samples, the one sintered at 800 °C showed a stable capacity of 620 mAh g^{-1} over 70 cycles at a rate of 0.1*C*. The optimized sample was used as an anode material with different binding agents such as polyvinylidene fluoride (PVDF), sodium carboxymethyl cellulose (NaCMC), lithium carboxymethyl cellulose (LiCMC), Xanthan Gum (XG), and Poly 3,4-ethlenedioxythiophene-poly-styrenesulfonate (PEDOT/PSS or Baytron). Among these agents, CMC-based salts and Baytron delivered the most stable capacities. In contrast, the use of PVDF and XG resulted in severe capacity fading [Figure 7(c)]. However, the Baytron binder, while highly conductive (10–500 mS cm^{-1}), is also expensive. The PVDF and XG binders could not accommodate the volume strain during the insertion–extraction process, so the electrical connections between the active material and current collector broke, leading to capacity fading. CMC-based salts alleviated the volume expansion during the cycling process, thus facilitating the improvement of the cycling stability. Li-based CMC resulted in a capacity of 690 mAh g^{-1} over 70 cycles at a rate of 0.1*C*, which is greater than the capacity that resulted from the use of Na-based CMC as it only provided a specific capacity of 615 mAh g^{-1} over 70 cycles. Furthermore, to analyze the effects of the electrolyte composition, a sample sintered at 800 °C and a LiCMC binder were used with different compositions of the electrolyte propylene carbonate (PC)-1 M lithium hexafluorophosphate ($LiPF_6$), ethylene carbonate (EC):dimethyl carbonate (DMC) (1:1)-1 M $LiPF_6$, and ethylene carbonate (EC):diethylene carbonate (DEC) (3:7)-1 M $LiPF_6$]. The specific capacity was increased for both EC:DMC (1:1) and EC:DEC (3:7) when the cycle number increased, but such a change did not occur with the PC-based electrolyte because PC does not contribute to a stable SEI layer and is also inactive for Li storage.[114] The EC:DEC electrolyte-composition capacity increased faster, as compared to that of the EC:DMC, as the former compound retained a specific capacity of 800 mAh g^{-1} after 100 cycles. This observation indicated that EC:DEC electrolyte promoted the faster formation of an SEI layer on the surface of the active material. Finally, the optimized sintered sample, LiCMC binder, and EC:DEC (3:7)-1M $LiPF_6$ (electrolyte) were used to fully fabricate a cell.

Furthermore, to attain a stable capacity and high rate capability, $ZnMn_2O_4$ has been synthesized in various morphologies such as mesoscale tubular arrays, porous microspheres, quasimesocrystal twin microspheres, loaf-like nanorods, and hybrid $ZnMn_2O_4$–graphene nanosheets.[115-119] Wang and coworkers reported porous $ZnMn_2O_4$ microspheres prepared through the calcination of metal carbonates via a solvothermal reaction [Figure 7(d)].[116] BET analysis indicated that the surface area and pore volume of these porous $ZnMn_2O_4$ microspheres were 17.7 m^2 g^{-1} and 0.27 cm^3 g^{-1}, respectively, indicating that the pores were in the range of 45 to 90 nm. Figure 7(e) shows the cycling performance of the $ZnMn_2O_4$ microspheres, analyzed in a potential window of 0.01–3 V at 500 mA g^{-1}. Over the first 50 cycles, the specific capacity decreased to 700 mAh g^{-1} after it had gradually increased, and it reached a value of 800 mAh g^{-1} on the 100th cycle, where it was maintained over 300 cycles. Figure 7(f) indicates that at a higher current density of 2000 mA g^{-1}, the capacity was maintained at 395 mAh g^{-1}. Overall, this excellent cycling stability and rate performance were achieved through the porous structures of the $ZnMn_2O_4$ microspheres, which provided high accessibility of the electrolyte over the electrode surface, high surface area that facilitated both charge transfer and a short diffusion distance for Li ions, and the alleviation of the pulverization problems during the insertion–extraction of Li^+ ions.

Compared to porous microspheres, solvothermally prepared quasimesocrystal $ZnMn_2O_4$ twin microspheres [Figure 7(g)] demonstrated better electrochemical performance [Figures 7(h) and 7(i)]. They demonstrated a high specific capacity of 484 mAh g^{-1} at a current density of 2 A g^{-1},[117] and current density return to 0.2 mA g^{-1} they exhibited a capacity of 1084 mAh g^{-1}. This excellent electrochemical performance was mainly attributed to the structural assembly, i.e., the twin microspheres that consisted of a 3D, porous, hierarchical structure composed of smaller primary nanoparticles that increased the number of active sites available for Li ions. The pores on the surfaces and within the interiors alleviated strain during the insertion–extraction process and provided a short diffusion path for Li ions, so an oriented mesocrystal could facilitate more electronic conductivity and in turn excellent specific capacity, cycling stability, and high rate capability. Xiong et al. reported the high rate capability of a $ZnMn_2O_4$ anode material using a 2D graphene nanoarchitecture prepared via a reflux method. The $ZnMn_2O_4$ nanoparticles uniformly distributed on the 2D nanosheet, forging a synergistic effect between the nanoparticles and graphene sheets that enhanced the conductivity and large active surface area, which maintained the structural integrity during the cycling process [Figure 7(j)]. Figures 7(k) and 7(l) show the astonishing properties of this 2D $ZnMn_2O_4$–graphene that had a stable capacity of 806 mAh g^{-1} at a low current density of 200 mA g^{-1}, but it still maintained a high specific capacity of 568 mAh g^{-1} even when the current density was increased to 3200 mA g^{-1}, indicating the high rate capability of these $ZnMn_2O_4$ nanoparticles with a graphene nanoarchitecture.[119] For simple comparison, the electrochemical performances of $CoMn_2O_4$ and $ZnMn_2O_4$ with various morphologies, synthesized via different techniques, are provided in Table 3.

Among the manganites, $ZnMn_2O_4$ exhibits a lower oxidation potential and higher cell-output voltage than $NiMn_2O_4$ and $CoMn_2O_4$. However, $ZnMn_2O_4$ exhibits a higher cell-output voltage than $ZnFe_2O_4$, since Fe has a higher oxidation potential (~1.61 V). Therefore, the synthesis of a large surface area with a proper composite is necessary to enhance the electrochemical performance of $ZnMn_2O_4$, and it may be expected to become a valuable source for Li ion anode materials for applications to LIBs.

View Article Online
DOI: 10.1039/C5RA23503K

3.3. ACo_2O_4 (*A* = Mg, Cu, Fe, Zn, Mn, and Ni)

Spinel cobaltites are an important group of spinel-type materials and have been widely investigated for use in applications in different fields such as sensors, bifunctional electrocatalysts, supercapacitors, and LIBs.[121-124] ACo_2O_4 has demonstrated excellent performances in LIBs, including such characteristics as high specific capacities, long cycle lives, and good rate capabilities, and it is slightly less toxic than Co_3O_4. Table 4 lists the electrochemical performances of spinel cobaltites. For the most part, spinel cobaltites store Li ions through a conversion-reaction mechanism except for $ZnCo_2O_4$, since it follows both the conversion and alloying–de-alloying mechanisms. Sharma et al. first investigated the electrochemical performance of $CuCo_2O_4$, $MgCo_2O_4$, and $FeCo_2O_4$, synthesized via a low-temperature urea-combustion method and an oxalate-decomposition method, for applications in LIBs. The electrochemical reaction was analyzed using cyclic-voltammetry analysis in the potential range of 0.005–3.0 V, and their reaction mechanisms are written as follows,[124-126]

$$MCo_2O_4 + 8Li^+ + 8e^- \rightarrow M + 2Co + 4Li_2O \text{ (M = Cu, Fe Ni, Mn)} \quad (22)$$

$$MgCo_2O_4 + 6Li^+ + 6e^- \rightarrow MgO + 2Co + 3Li_2O \quad (23)$$

$$M + Li_2O \leftrightarrow MO + 2Li^+ + 2e^- \quad (24)$$

$$2Co + 2Li_2O \leftrightarrow 2CoO + 4Li^+ + 4e^- \quad (25)$$

$$2CoO + 2/3Li_2O \leftrightarrow 2/3Co_3O_4 + 4/3Li^+ + 4/3e^- \quad (26)$$

After the first discharge, $MgCo_2O_4$ converted into MgO, which was then no longer involved in the reaction mechanism, since it acted as an inactive matrix and avoided the volume expansion. Galvanostatic-cycling studies indicated that $MgCo_2O_4$ demonstrated serious capacity fading, i.e., it retained only a very small capacity of 108 mAh g^{-1} after 50 cycles.[125] On the other hand, $CuCo_2O_4$ and $FeCo_2O_4$ possessed reasonable discharge capacities of 745 and 752 mAh g^{-1}, respectively, after 50 cycles. These results might be due to the conversion reactions of both the *A*- and *B*-site metal cations. In contrast, only the *B*-site cations contributed to the charge storage in $MgCo_2O_4$.

Among these cobaltites, $ZnCo_2O_4$ has received much attention as a potential material for anodes in LIBs. In the $ZnCo_2O_4$-spinel structure, Zn^{2+} ions occupy the tetrahedrally coordinated sites, and Co^{3+} ions occupy the octahedrally coordinated sites, and this structure involves an overarching electrochemical reaction through a conversion reaction between the Co and Zn ions and an alloying reaction between the Zn and Li that provides the overall charge-storage capacity. This reaction mechanism is given as,[127-131]

$$ZnCo_2O_4 + 8Li^+ + 8e^- \rightarrow Zn + 2Co + 4Li_2O \quad (27)$$

$$Zn + Li^+ + e^- \leftrightarrow LiZn \quad (28)$$

$$Zn + Li_2O \leftrightarrow ZnO + 2Li^+ + 2e^- \quad (29)$$

$$2Co + 2Li_2O \leftrightarrow 2CoO + 4Li^+ + 4e^- \quad (30)$$

$$2CoO + 2/3Li_2O \leftrightarrow 2/3Co_3O_4 + 4/3Li^+ + 4/3e^- \quad (31)$$

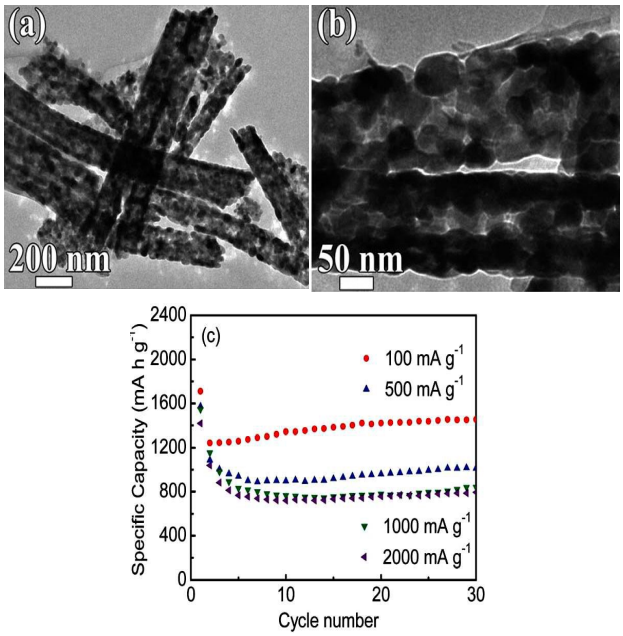

Figure 8. (a, b) Porous $ZnCo_2O_4$ nanotubes and (c) their cycles at different current densities. (Reproduced from Ref. 128. Copyright 2012, with permission from the royal society of chemistry.)

$ZnCo_2O_4$ has been widely investigated, and to study its electrochemical performance, researchers have reported various morphologies, including nanotubes,[128] 3D hierarchical nanowires,[129] uniform mesoporous microspheres,[132] and yolk-shelled microspheres,[133] and they have also grown it on different current collectors, including Ni foam and carbon cloth.[131, 134] Importantly, porous $ZnCo_2O_4$ nanotubes, synthesized via an electrospinning technique with subsequent heat treatment. Figures 8(a) and 8(b) show the nanotubes (~200 nm), which consist of interconnected primary nanocrystals (~30 nm) and nanopores (~3 nm) in the walls which exhibited a capacity of 1454 mAh g^{-1} at 100 mA g^{-1} over 30 cycles with 100% Coulombic efficiency (Figure 8(c)).[128] Even at high current densities of 500, 1000, and 2000 mA g^{-1}, they demonstrated high reversible capacities of 1011, 841, and 794 mAh g^{-1}, indicating that these porous nanotubes could accommodate the volume strain and that the well-interconnected nanoparticles shortened the pathway of Li ion diffusion and enhanced the electronic conductivity, and they possessed large surface areas that led to an increase in the active sites for Li ion diffusion. Liu et al. reported a binder- and current-collector-free 3D hierarchical $ZnCo_2O_4$ nanowire array grown on flexible carbon cloth using a hydrothermal method.[129] Figure 9(a) depicts its schematic diagram, while Figures 9(b)–9(e) depict the morphologies of the well-ordered

View Article Online
DOI: 10.1039/C5RA23503K

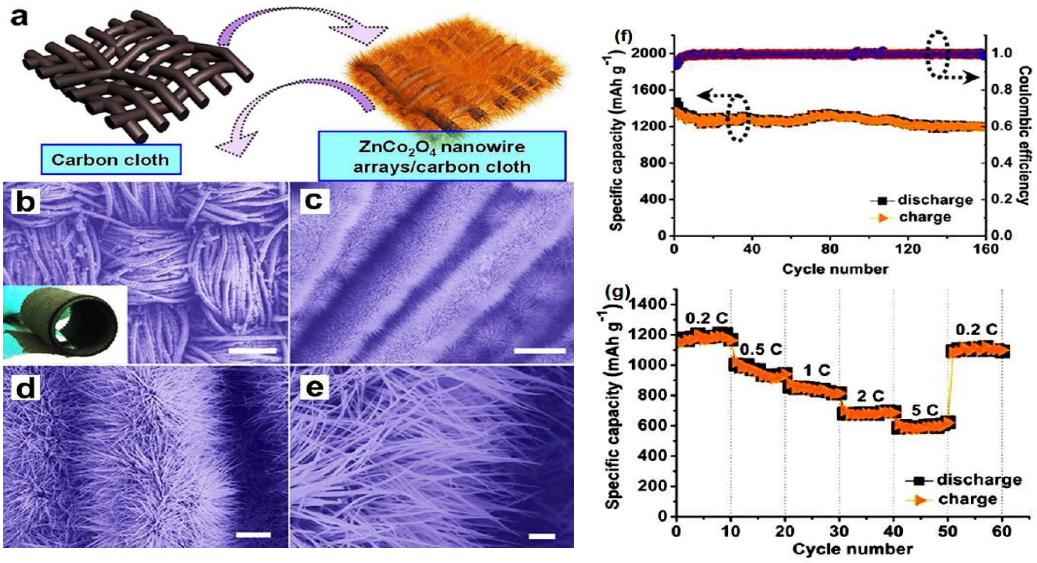

Figure 9. (a) Schematic diagram of a $ZnCo_2O_4$ nanowire array on carbon cloth. (b)–(e) Morphologies of these $ZnCo_2O_4$ nanowires. (f) and (g) Their cycling stability and different current densities. (Reprinted with permission from ref. 129. Copyright 2012, American Chemical Society)

woven structure of the array on carbon cloth in which the $ZnCo_2O_4$ nanowires have uniform diameters of 80-100 nm and lengths of 5 μm. Figure 9(f) shows the cycling-stability curve at 200 mAh g^{-1}. This array had a high irreversible capacity of 1530 mAh g^{-1} over the initial cycles. After 50 and 100 cycles, it possessed capacities of 1280 and 1278 mAh g^{-1}, respectively, with 99% capacity retention, and still it retained a stable specific capacity of about 1200 mAh g^{-1} after 160 cycles. The reported capacity was very high when compared with the theoretical specific capacity due to the reversible growth of a polymeric/gel-like film on the surface of the active material.[130] The current density rises upto 5C rate it maintain the stable capacity of 605 mAh g^{-1} (Figure 9(g)). The superior electrochemical performance of $ZnCo_2O_4$ on carbon cloth depended primarily on the following factors. The $ZnCo_2O_4$ nanowires strongly adhered to the carbon cloth, facilitating good electronic conductivity, and the open spaces between the nanowires accommodated the volume strain and allowed electrolyte penetration into the active materials, leading to an increase in the number of active sites. The nanowires also shortened the Li^+ ion diffusion path, enhancing the rate capability. It has been suggested that binder- and current-collector-free flexible $ZnCo_2O_4$ nanowires on carbon cloth are a good candidate for flexible LIBs.

In addition to that of $ZnCo_2O_4$, the Co-based-spinel structures of $MnCo_2O_4$ and $NiCo_2O_4$ have also been widely examined,[136-139] as Mn-based cobaltite ($MnCo_2O_4$) is considered a promising candidate for LIBs due to its low cost, environmental benignity, and lower operating voltage.[140] Recently, Li et al. reported the electrochemical performance of stoichiometric $MnCo_2O_4$-spinel mesoporous microspheres prepared via a one-step low-temperature solvothermal method. The microspheres showed a discharge capacity of 722 mAh g^{-1} over 25 cycles at 200 mA g^{-1}. Due to the hierarchical structure of $MnCo_2O_4$,[141] they demonstrated a superior rate-capability performance. Qian et al. prepared core–shell $Mn_{1.5}Co_{1.5}O_4$ with a nonstoichiometric, spinel structure via a solvothermal route and reported its discharge capacity of 618 mAh g^{-1} at 400 mA g^{-1} with good cycling stability even after 300 cycles.[142] Interestingly, Shen et al. fabricated the hierarchical structure of $MnCo_2O_4$ nanosheet arrays on carbon cloth [Figures 10(a)–10(c)] that demonstrated excellent electrochemical performance, which was even better than that of Co_3O_4 on carbon cloth[140] since the carbon cloth assured good electronic conductivity between the active material and the current collector. Therefore, this type of binder- and additive-free electrode is a promising anode material for LIBs.

Similarly, $NiCo_2O_4$ has also been exploited as an efficient energy-storage material for diverse applications, including bifunctional electrocatalysts, supercapacitors, and LIBs.[122, 143, 144] It exhibits a high electronic conductivity due to the mixed valences of the same cations in the metal oxides. $NiCo_2O_4$ [$Co^{2+}_{1-x}Co^{3+}[Co^{3+}Ni^{2+}_xNi^{3+}_{1-x}]O_4$] exhibits two- to three-fold increases in the electrical conductivity, compared to simple metal oxides. For example, the electrical conductivity of Co_3O_4 is 3.1×10^{-5} S. cm^{-1}, and that of $Ni_xCo_{3-x}O_4$ is 0.1–0.3 S. cm^{-1}. Hence, the high electronic conductivity of $NiCo_2O_4$ enhances the rate capabilities and cycle lives of LIBs.[145, 146] Park and his group recently reported the excellent electrochemical performance of urchin-like, mesoporous [Figure 11(a)] $NiCo_2O_4$ spinel, which was synthesized via a simple, cost-effective coprecipitation method followed by a low-temperature calcination process.[145]

View Article Online
DOI: 10.1039/C5RA23503K

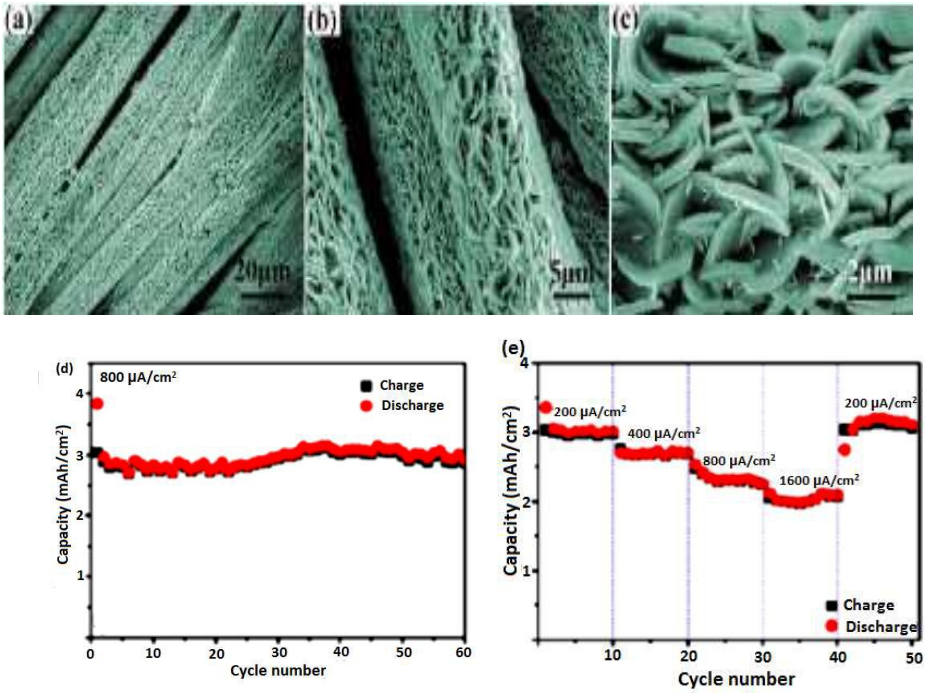

Figure 10. (a)–(c) Morphologies of $MnCo_2O_4$ nanosheet arrays on carbon cloth. (d) Their cycling stability and (e) rate-capability curve. (Reproduced from Ref. 140. Copyright 2014, with permission from the royal society of chemistry.)

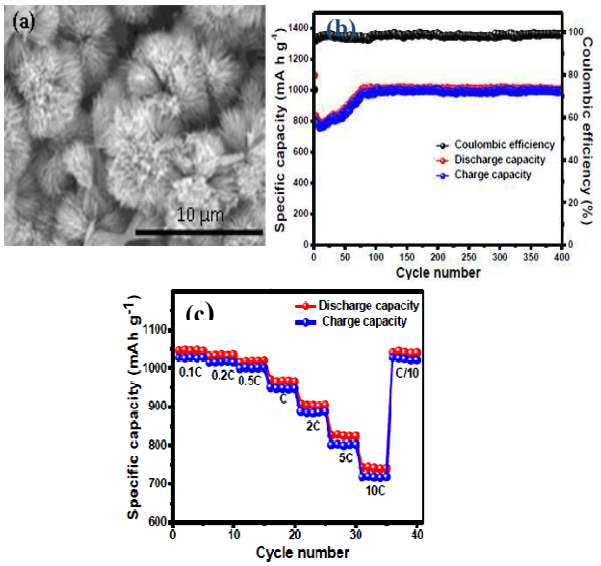

Figure 11. (a)–(c) Urchin-like morphology of $NiCo_2O_4$, its cycling stability curve at a 0.1*C* rate, and its current densities at different *C* rates. (Reproduced from Ref. 145. Copyright 2014 with permission from the royal society of chemistry.)

It possessed a discharge capacity of 1000 mAh g^{-1} after 400 cycles at a current rate of 0.1C with a high Coulombic efficiency greater than 98%, and it showed an extraordinary rate capability [Figures 11(b) and 11(c)]. Instead of conventional PVDF, they used PAA as a binder as it could accommodate the volume strain due to its elastic nature and could assist the efficient electronic conductivity between the active material and the current collector.

From the observation of these cobaltites, urchin-like mesoporous $NiCo_2O_4$ demonstrated an excellent electrochemical performance without any composites because its good electronic conductivity and mesoporous structure led to a high rate capability and high specific capacity. To further improve the electronic and Li ion transports of the urchin-like $NiCo_2O_4$, a composite containing carbonaceous material is necessary.

4. Germanates, stannates, and silicates, A_2BO_4 (*A* = Zn, Co, Mn, and Co; *B* = Ge, Sn, Si, and Ti)

It is believed that Zn_2GeO_4 is an efficient anode material, since ZnO and GeO_2 are electrochemically active for Li ion storage through the alloying–de-alloying-reaction mechanism and they exhibit high reversible capacities of 978 and 1100 mAh g^{-1}, respectively.[160, 161] Ge has 400 and 10,000 times greater Li diffusivity and electronic conductivity, respectively, than Si, but during the alloying–de-alloying process, it undergoes a volume change of up to 260% that leads to cracks in the electrode material.[162, 163] Therefore, to avoid the aggregation

View Article Online
DOI: 10.1039/C5RA23503K

of Ge particles and reduce the cost of the electrode material, some active metal oxides such as BaO, CaO, and ZnO have been implemented.[160-162] Among these compounds, BaO and CaO act as inactive matrices that reduce the capacity of the material, but ZnO facilitates Li storage and prevents particle aggregation. The alloying–de-alloying-reaction mechanism of Zn_2GeO_4 is,[162, 163, 166-168]

$$Zn_2GeO_4 + 8Li^+ + 8e^- \rightarrow 2Zn + Ge + 4Li_2O \quad (32)$$

$$Zn + xLi^+ + xe^- \leftrightarrow Li_xZn\ (0 \le x \le 1) \quad (33)$$

$$Ge + yLi^+ + ye^- \leftrightarrow Li_yGe\ (0 \le y \le 1) \quad (34)$$

$$Zn + Li_2O \leftrightarrow ZnO + 2Li^+ + 2e^- \quad (35)$$

$$Ge + 2Li_2O \leftrightarrow GeO_2 + 4Li^+ + 4e^- \quad (36)$$

Feng and coworkers analyzed the electrochemical performance of Zn_2GeO_4 nanorods, synthesized via a hydrothermal method,[162] and obtained a discharge capacity of 1820 mAh g^{-1} in the first cycle, but this value linearly decreased to 616 mAh g^{-1} after 100 cycles. Therefore, to further enhance the specific capacity and cycling stability, they synthesized amorphous nanoparticles and graphene composite with the Zn_2GeO_4 particles in order to overcome the volume expansion and enhance the conductivity of the electrode material.[163, 166-168] The amorphous phase of the Zn_2GeO_4 nanoparticles showed a high reversible capacity of 1250 mAh g^{-1} at 400 mA g^{-1} over 500 cycles, and the capacity was maintained at 470 mAh g^{-1} at 6400 mA g^{-1}. The high specific capacity and rate capability resulted from the facts that the amorphous structure did not suffer from stresses that mitigated the pulverization of the material and that the incorporation of Zn and oxygen acts as a buffering matrix, thus contributing to the reversible capacity.[166]
The Huang group reported sandwiched Zn_2GeO_4–graphene-oxide nanocomposites using an ion-exchange-reaction method [Figure 12(a)].[163] Among these composites, 12.1 wt% of the Zn_2GeO_4–graphene-oxide nanocomposite showed a good cycling stability, had a specific capacity of 1150 mAh g^{-1} at 200 mA g^{-1} over 100 cycles, and maintained a stable capacity of 568 mAh g^{-1} at a high current density of 3.2 A g^{-1}, as shown in Figures 12(b) and 12(c). These Zn_2GeO_4 nanorods were completely wrapped in the graphene oxide, which thereby accommodated the strain from the volume expansion and preserved the integrity of the active material, thus leading to the improved mobilities of the ions and electrons. Recently, the Wang group explored Fe_2GeO_4 as an anode material for LIBs, as it has shown excellent electrochemical performance. Fe_2GeO_4 exhibits a high theoretical specific capacity of 1119 mAh g^{-1}, according to the following electrochemical reactions,

$$Fe_2GeO_4 + 8Li^+ + 8e^- \rightarrow 2Fe + Ge + 4Li_2O \quad (37)$$

$$2Fe + 3Li_2O \leftrightarrow Fe_2O_3 + 6Li + 6e^- \quad (38)$$

$$Ge + 4.4Li^+ + 4.4e^- \leftrightarrow Li_{4.4}Ge \quad (39)$$

Figure 12(d) shows the TEM image of an Fe_2GeO_4–graphene composite that had a capacity of 980 mAh g^{-1} at 360 mA g^{-1} after 175 cycles and a high reversible capacity of 340 mAh g^{-1} at 4800 mA g^{-1} is shown in figure 12(e).[27] This type of A_2BO_4 structure has some advantages, as the first lithiation evenly distributed between the Li_2O matrix and the metal particles. Here, Li_2O acts as a buffering matrix, as it can effectively accommodate the volume strain, and the secondary metal nanoparticles enhance the electrical conductivity of the electrode material. These factors lead to electrode materials with both good cyclabilities and good rate performances.[169] Zhang et al. first reported a Co_2GeO_4@reduced-graphene composite as a Li ion anode material that demonstrated a specific capacity of 1085 mAh g^{-1} over 100 cycles with cycling stability superior to that of Co_2GeO_4. Reduced-graphene oxide (rGO) served as a good electronic conductor between the particles and an excellent buffering matrix to accommodate the volume strain during the charge–discharge process. Co_2GeO_4 combined with rGO specifically demonstrated a high specific capacity, good rate capability, and cycling stability.[167] Among the germanates, Zn_2GeO_4 is considered an ideal anode material for LIBs because of its low working potential and high energy density, and the reduced usage of Ge is also beneficial in reducing the cost of the material (27% of Ge in Zn_2GeO_4) compared to other Ge-based materials.[171]

A different set of mixed-metal oxides that contain Sn is another group of important prospects for improving the specific capacity of an electrode material. Metal stannates (M_2SnO_4; M = Mn, Co, Zn) store Li ions through both a conversion-reaction mechanism and an alloying–de-alloying mechanism as follows,[30, 172-175]

$$M_2SnO_4 + 8Li \rightarrow 2M + 4Li_2O + Sn\ (M = Mn, Co) \quad (40)$$

$$Sn + 4.4Li \leftrightarrow Li_{4.4}Sn \quad (41)$$

$$Sn + 2Li_2O \leftrightarrow SnO_2 + 4Li \quad (42)$$

$$M + Li_2O \leftrightarrow MO + 2Li \quad (43)$$

Lei et al. prepared ultrafine Mn_2SnO_4 nanoparticles using the thermal decomposition of a $MnSn(OH)_6$ precursor.[174] The Mn_2SnO_4 nanoparticles showed severe capacity fading upon cycling due to volume expansion. During the alloying–de-alloying process, Sn metal expands up to 200–300% (volume expansion), causing peeling of the active material and breaking the electronic conductivity between the active material and the current collector. A similar type of capacity was observed for Co_2SnO_4 nanoparticles, synthesized via a facile hydrothermal method, which had a capacity of 555 mAh g^{-1} after 50 cycles at 30 mA g^{-1} with a capacity retention of 50.3%,

View Article Online
DOI: 10.1039/C5RA23503K

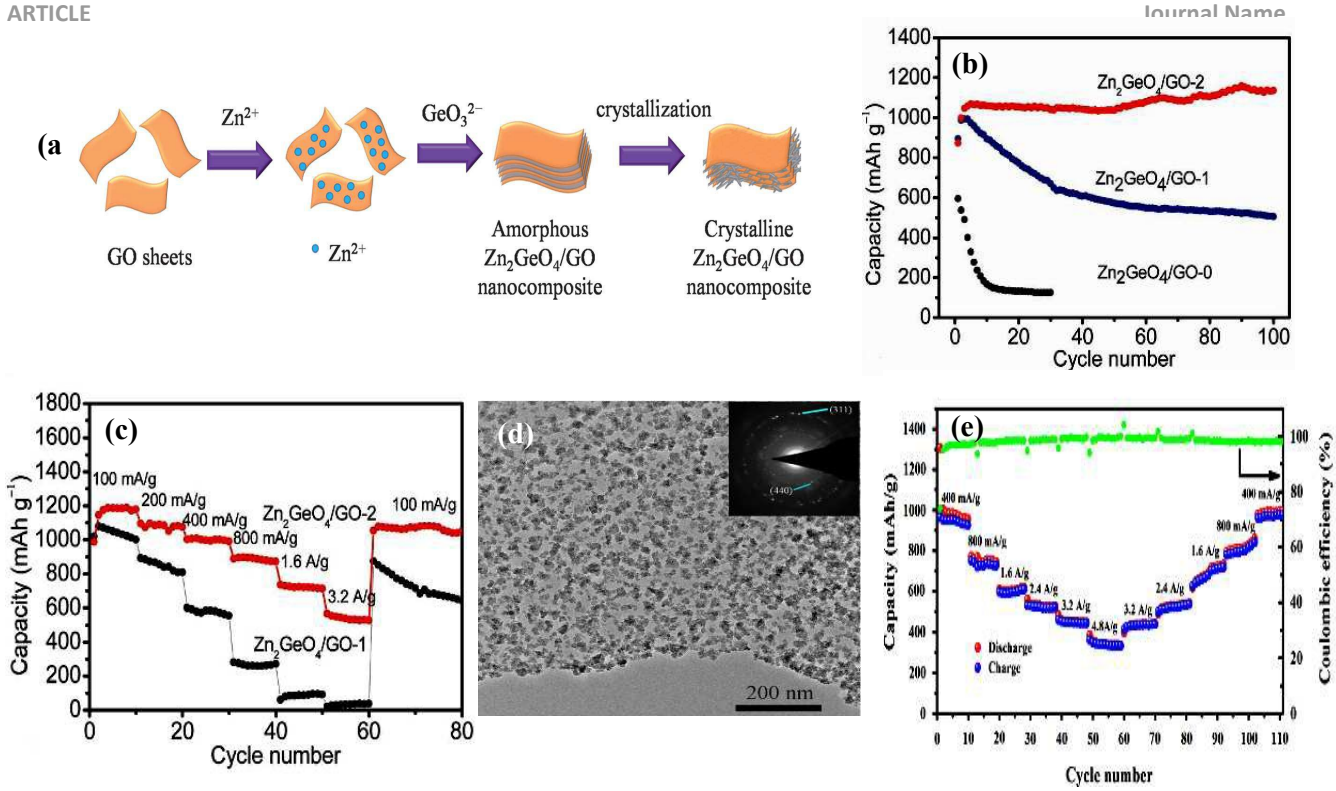

Figure 12. (a) Schematic diagram of Zn_2GeO_4–graphene-oxide nanocomposites. (b) Cycling-stability curve at 200 mA g^{-1} at different weight percentages of carbon and (c) the rate-capability curve. (Reproduced from Ref. 163. Copyright 2014, with permission from the royal society of chemistry.) (d) TEM image of an Fe_2GeO_4–graphene composite and (e) its rate-capability curve. (Reprinted with permission from ref. 27. Copyright 2014 Elsevier.)

and even after 50 cycles, they still could not attain a stable capacity.[176] To overcome this drawback, a Co_2SnO_4@C core–shell structure, a composite with MWCNTs and Co_2SnO_4 wrapped with graphene, was analyzed to enhance the electrochemical performance of the Co_2SnO_4.[177-180] Qi and coworkers reported that the core–shell structure of Co_2SnO_4@C, prepared through a hydrothermal process, with different thicknesses of carbon coating (10.5 and 25.2 wt%) was achieved using glucose as the carbon source. Among these materials, the one with the thick carbon coating showed a high discharge capacity of 474 mAh g^{-1} with a capacity retention of 60.4% after 75 cycles, a value that was greater than that of the one with the thin carbon coating (173 mAh g^{-1}).[177] The cycling stability of Co_2SnO_4 was attributed to the core–shell structure of Co_2SnO_4@C, and it had several advantages such as stable SEI-film formation, a lack of aggregation with the active material, the enhancement of the electrical conduction with the active material, and functioning as a buffering matrix during the charge–discharge process.[178] CNTs are also considered to be important carbonaceous materials that enhance the electrochemical performances of metal oxides, and they have various attractive features, including excellent electrical conductivity, a large length versus diameter ratio, a large surface area, structural flexibility, and chemical stability.[179, 181, 182] Liu and his group proposed a multiwalled-carbon-nanotube (MWCNT) composite with Co_2SnO_4 nanoparticles that possessed a stable capacity of 898 mAh g^{-1} at 50 mAg^{-1} over 50 cycles.[179] Compared to the Co_2SnO_4 nanoparticles, the Co_2SnO_4–MWCNT composite showed good reversibility with feeble capacity fading that was due to its highly conductive matrix of MWCNTs that facilitated contact between the nanoparticles, accommodated the volume expansion, and prevented the aggregation of nanoparticles during the cycling process.[183, 184] Recently, Zhang and his groups reported Co_2SnO_4 hollow cubes@rGO, synthesized via the pyrolysis-induced transformation from the hollow, cubic precursor prepared via a hydrothermal method, where the composite with graphene sheets was attained through an electrostatic-interaction mechanism.[180] Figures 13(a–d) and Fig 13(e, f) show the schematic diagram and TEM images of hollow Co_2SnO_4 cubes with graphene composite, which exhibit excellent electrochemical performance, as compared to the core–shell structure and the MWCNT composite.[179, 180] The BET analysis indicated that the Co_2SnO_4 hollow cubes@rGO exhibited a high surface area of 62.88 m^2 g^{-1} that facilitated an interfacial electrochemical reaction. Figure 13(g) depicts the discharge capacity versus cycle number and indicates that the specific capacity of Co_2SnO_4 hollow cubes@rGO was 1126 mA h g^{-1} at 100 mA g^{-1} after 50 cycles. This value was greater than the theoretically calculated value (1105 mAh g^{-1}), a discrepancy that resulted from either the interfacial-charge storage or the thick-SEI-film formation,[108, 185] and this material maintained its capacity of 1016 mAh g^{-1} after even 100 cycles. For practical applications, they varied the mass loading from 1–2 mg to 5–6 mg, but no obvious change was observed in the cycling process; the discharge capacity was only reduced to 40 mAh g^{-1}, compared to that of the low mass loading. In Figure 13(h), the

View Article Online
DOI: 10.1039/C5RA23503K

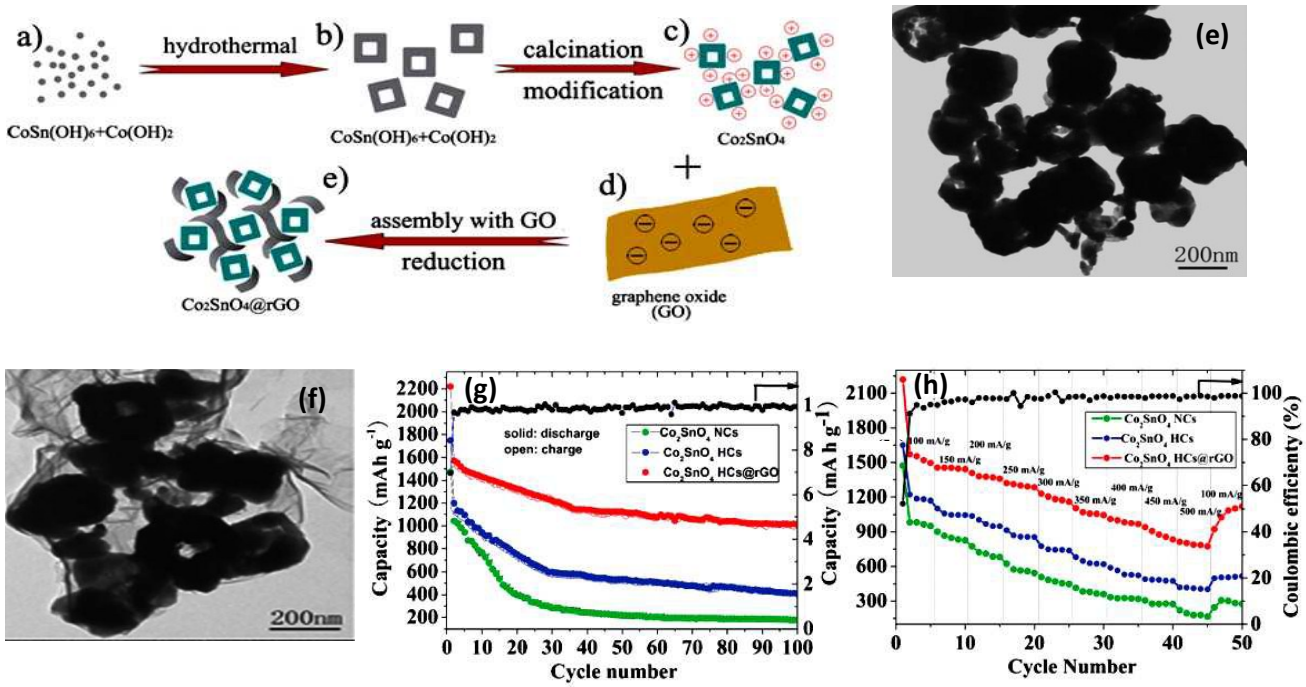

Figure 13. (a–d) and (e, f) Schematic diagram of Co_2SnO_4–graphene-composite formation and its corresponding TEM images respectively. (g) The cycling stability and (h) rate capability of Co_2SnO_4 nanocrystals, hollow cubes, and graphene composite. (Reproduced from Ref. 180. Copyright 2014, with permission from the royal society of chemistry.)

Co_2SnO_4 hollow cubes@rGO had a greatly enhanced rate capability of 775 mAh g^{-1} at a current density of 500 mA g^{-1}.

The electrochemical performance was mainly attributed to the hollow cubes of Co_2SnO_4 and the combined effects of the graphene nanosheets. Both the hollow cubes and the graphene could accommodate the volume expansion and contraction during the charge–discharge process, thereby facilitating the extra capacity from the interfacial storage of Li ions and graphene, improving the conductivity between the particles, and thus leading to a good rate capability of the active material.

Zn_2SnO_4 belongs to an inverse-spinel group (space group *Fd3m*) with a band gap of 3.6 eV, and it possesses high electron mobility, high electron conductivity, and low visible absorption.[186, 187] Due to these astonishing properties, it has been widely investigated for applications in different fields such as gas sensors, solar cells, and photocatalysts.[188-190] Apart from these studies, Zn_2SnO_4 has mainly been investigated as a Li ion anode material due to the low working potentials of ZnO (0.05–1.50 V) and SnO_2 (0–1.0 V) as well as their high specific capacities of 980 and 780 mAh g^{-1}, respectively.[191, 192] Both Zn and Sn are electrochemically active and are involved in the charge-storage mechanism through the alloying mechanism (Li–Zn and Li–Sn), and they could accommodate 14.4 Li ions in the first cycle, demonstrating an irreversible capacity of 1231 mAh g^{-1} and exhibiting a reversible capacity of 547 mAh g^{-1}, according to the electrochemical-reaction mechanism,[193-195]

$$Zn_2SnO_4 + 4Li^+ + 4e^- \rightarrow Sn + 2Li_2O + 2ZnO \quad (44)$$

$$Zn_2SnO_4 + 8Li^+ + 8e^- \rightarrow 2Zn + Sn + 4Li_2O \quad (45)$$

$$Sn + xLi^+ + xe^- \leftrightarrow Li_xSn, (x \leq 4.4) \quad (46)$$

$$Zn + yLi^+ + ye^- \leftrightarrow Li_yZn, (y \leq 1) \quad (47)$$

During the charge–discharge process, the Zn_2SnO_4 material undergoes a large volume change, but it cannot accommodate the volume strain during the cycling process, thus leading to severe capacity fading.[193-195] Therefore, many efforts have been made to improve the cycling stability and specific capacity of Zn_2SnO_4, so particles have been synthesized in different shapes, including cubes, hollow cubes, wires, nanoplates, hollow nanospheres, composites with carbon, graphene metal–organic frameworks, and conducting polymers,[187, 194, 196-204] and their electrochemical performances are listed in Table 5. Zhang et al. developed hollow Zn_2SnO_4 nanospheres [Figure 14(a)] via a hydrothermal method followed by an annealing process, and these hollow nanospheres exhibited a high surface area of 42.53 m^2 g^{-1} and

View Article Online
DOI: 10.1039/C5RA23503K

pore volume of 0.24 cm^3 g^{-1}.[197] Figures 14(b) and 14(c) depict these hollow nanospheres with a capacity of 602 mAh g^{-1} at 100 mA g^{-1} over 60 cycles and 442 mAh g^{-1} even at 1000 mA g^{-1} after 60 cycles. Therefore, this superior electrochemical performance of the hollow nanospheres resulted from different factors, including their large surface areas, enlarging the electrolyte–electrode-contact area and porous structure that allowed the electrolyte into the electrode, increasing the active sites for Li storage and accommodating the volume strain during the charge–discharge process. Recently, hollow Zn_2SnO_4 boxes@carbon/graphene ternary composite was prepared via a hydrothermal method followed by a calcination process.[198] Figures 14(d) and 14(e) show the TEM image of the ternary composite and its electrochemical performance, and it exhibited high irreversible discharge capacities of 1863 and 1256 mAh g^{-1} on the first two cycles. The discharge-capacity values were large compared to the theoretical specific capacity, a result that is due to the extra Li storage on the active material through a pseudocapacitance mechanism.[205]

The ternary composite retained a capacity of 726 mAh g^{-1} at 300 mA g^{-1} over 50 cycles, and when the current density increased to 1200 mA g^{-1}, it maintained a capacity of 438 mAh g^{-1} (Figure 14(f)). The ternary composite exhibited an excellent cycling stability and rate performance, as compared to those of hollow Zn_2SnO_4 boxes wrapped with flexible graphene.[198, 200] Therefore, their excellent electrochemical performance was attributed to their hollow structure, carbon layer, and graphene composite, which act as a triple buffering structure, efficiently accommodating the volume strain during alloying–de-alloying process. Additionally, the carbon layer and graphene composite enhanced the electronic conductivity of the composite and thus improved the rate capability of the material. Overall, it can be concluded that the Zn_2SnO_4@graphene composite showed linear capacity fading during the cycling process but that Co_2SnO_4 showed a high reversible capacity. Nonetheless, the synthetic process of Co_2SnO_4 is difficult because of the high temperature it requires.[178]

Silicate-based mixed-metal oxides have also been analyzed for their potential applications to Li ion anode materials. Only a few reports are currently available that analyze silicate-based materials like Zn_2SiO_4 and Co_2SiO_4, but these materials do not exhibit high specific capacities compared to that of Co_3O_4.[206, 207] Zhang et al. reported Zn_2SiO_4 nanorods using a facile hydrothermal method, but they possessed a capability of only 388 mAh g^{-1} at 50 mA g^{-1} after 20 cycles with that capacity fading on subsequent cycles.[206] Muller and coworkers first reported an orthorhombic α-Co_2SiO_4 structure, prepared through a solid-state reaction, and examined its electrochemical performance as a Li ion anode material.[207]

From the cyclic voltammetry, in situ XRD analysis, and XPS results, they deduced the following reaction mechanism,

$$Co_2SiO_4 + 4Li^+ + 4e^- \rightarrow 2Co + Li_4SiO_4\,, \qquad (48)$$

$$x\mathrm{Co} + Li_4SiO_4 \leftrightarrow 4Li^+ + 4e^- + Co_xSiO_4. \qquad (49)$$

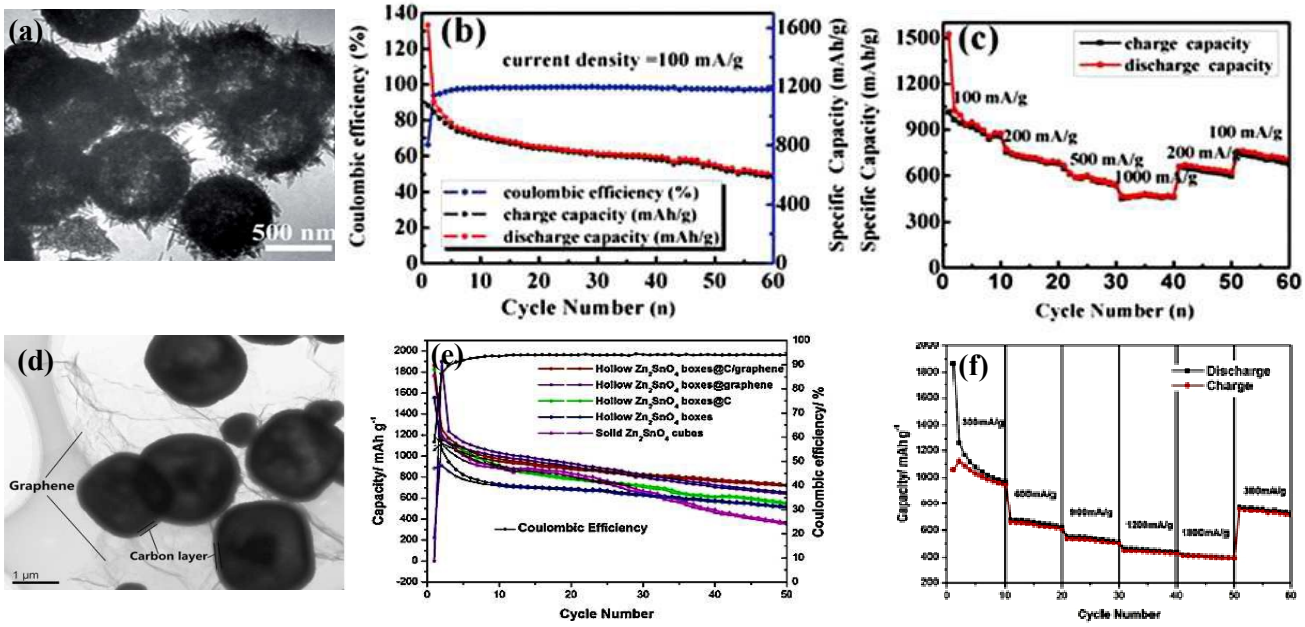

Figure 14. (a)–(c) Hollow Zn_2SnO_4 nanospheres, their cycling stability at 100 mA g^{-1}, and different current densities, respectively. ((Reproduced from Ref. 197. Copyright 2014, with permission from the royal society of chemistry.) (d)–(f) Zn_2SnO_4 ternary composite, cycling stabilities of different morphologies of Zn_2SnO_4 and its composites, and their stabilities at different current densities of the ternary composite. (Reprinted with permission from ref. 198. Copyright 2014 Elsevier.)

The reported reversible formation of Li_4SiO_4 enhances the Li ion conductivity that facilitates the high rate capability of the active material and yields a capability of 370 mAh g^{-1} at a high current density of 1580 mA g^{-1}. However, exploring the

View Article Online
DOI: 10.1039/C5RA23503K

detailed electrochemical performances of such silicate-based mixed-metal oxides is still necessary. For instance, Co_2SiO_4 and Zn_2SiO_4 materials yield SiO_2 and Li_4SiO_4 during the first discharge processes, respectively, so they are not involved in the electrochemical reactions, leading to low specific capacities and difficulties attaining pure phase formations.[208, 209] Therefore, it is mandatory to discover alternative anode materials apart from those mentioned above.

5. Role of Binder

In Li-ion batteries, binder plays a crucial role to improve the electrochemical performances. It is used as glue, which interconnected the active material and conducting agent that ensures the electronic conductivity between the active materials and the current collector.[210] The commercially used PVDF has several drawbacks, *i.e.,* low electronic conductivity, toxic and it dissolves in expensive organic solvent of NMP. Similarly, it could not accommodate volume change during charging-discharging process and adsorb more electrolyte ions that lead to high irreversible capacity loss during first cycle. Therefore, it creates an new avenue to identify an alternate binder instead of PVDF having the characteristics features including water soluble, low cost, high elasticity nature, high electronic conductivity and environmentally friendly.[211, 212] In this regard, recently many groups have identified different water soluble binders such as CMC (Carboxy methyl cellulose), SBR (Styrene butadiene rubber), PAA (Polyacrylic acid) and SA (Sodium alginate) for the applications of Li-ion batteries. CMC is a polymeric derivative of cellulose which consists of carboxylate anion and hydroxyl functional groups and these groups makes CMC as a water-soluble binder. Similarly, SBR is an elastomer, which has high flexibility, stronger binding force and better heat resistance than PVDF.[213] On the other hand, PAA is an environmentally friendly and it not only soluble in water it also soluble in organic solvent like ethanol. It has high concentration of functional groups which can give spacing between them through copolymerization with other monomers. The copolymerization of PAA offer many properties including, elastic modulus, maximum elongation, swelling in electrolyte, surface chemistry and the strength of adhesion between the active material and current collector.[80] The SA is a high modulus polysaccharide derived from brown algae which mainly consists of copolymer of 1→4 linked β-D-mannuronic acid (M) and α-L-guluronic acid (G) residues.[214] It has several advantages including ~6.7 times higher stiffness than dry films of PVDF, small swelling of electrolyte in its structure which restricts the undesirable reaction with the electrode/electrolyte interface, polar hydrogen bonds between the carboxyl groups in the binder that leads to strong adhesive between the active material and current collector and exhibits self healing effect during charging-discharging process.[214, 215] The following literatures are well depicted the importance of binders. Wei groups have reported that electrochemical performance of $ZnFe_2O_4$ using both PVDF and SBR/CMC as binders.[213] $ZnFe_2O_4$-SBR/CMC delivered high capacity of 627.6 mAh g^{-1} at 1C rate, which was much larger than that of $ZnFe_2O_4$-PVDF (144.9 mAh g^{-1}). Similarly, Yolk-shelled microsphere $ZnCo_2O_4$, delivered the stable specific capacity of 718 mAh g^{-1} and 325 mAh g^{-1}, while using CMC and PVDF, respectively as binders over 100 cycles. The result assured that SBR/CMC is a better choice for replacing PVDF, since SBR/CMC makes a unique three dimensional network between the active materials, which enhanced the stability of the electrode during cycling process.[133, 216] Wang group have analyzed the electrochemical performance of amorphous Zn_2GeO_4 nanoparticles using PAA as a binder.[166] The amorphous $ZnGe_2O_4$ nanoparticles showed the high reversible specific capacity of 1250 mAh g^{-1} over 100 cycles and it exhibited the high discharge capacity of 610 mAh g^{-1} at the high current density of 3.2 A/g. This excellent electrochemical performance was mainly attributed to the combined effect of amorphous Zn_2GeO_4 nanoparticles and PAA binder. Yushin group has first time introduced the sodium alginate as a binder for high capacity silicon nanopowder based lithium ion batteries.[81] Mitra groups recently evaluated the electrochemical performance of spinel $CoFe_2O_4$ nanoparticles using sodium alginate binder which exhibits the stable discharge capacity of 890 mAh g^{-1} over 50 cycles but using PVDF it stabilized at 160 mAh g^{-1} over 50 cycles. On the other hand, PAA used $CoFe_2O_4$ electrode delivered 470 mAh g^{-1} even at high current density of 20 C.[217] Similarly, Wang group reported the Co_2GeO_4 nanosheets for anode materials using sodium alginate as a binder that could possess stable capacity of 1026 mAh g^{-1} over 150 cycles. So, this excellent electrochemical performance such as cyclability and rate capability mainly attributed to the peculiar properties of sodium alginate binder.[29] Overall binders, the sodium alginate shows the good cycling stability and high rate capability compared to other so it is one the best binder to construct the Li-ion batteries.

6. Summary and outlook

In this overview, numerous research has been examined that focuses on the electrochemical performances of AB_2O_4- and A_2BO_4-structured materials and their corresponding pristine materials and that expounds on the large electrode polarization, high irreversible capacity loss, and unstable SEI-film formation that lead to poor cycling stability and rate capability. Hence, to achieve better electrochemical performances, researchers have focused on different strategies as summarized here. (i) The electrode materials have been prepared in different morphologies such as nanoparticles, hierarchical structures, nanowires, and nanotubes using different synthetic methods, including hydrothermal, solvothermal, thermal decomposition, and coprecipitation. (ii) Pristine materials have been composited

View Article Online
DOI: 10.1039/C5RA23503K

with carbonaceous compounds such as core–shells of carbon and graphene. (iii) Binders such as CMC, PAA, and sodium alginate also play an important role in facilitating the electrochemical performance. (iv) Finally, electrolyte additives such as Fluoroethylene carbonate (FEC) also contribute to cycling stability.

The first potential approach, *i.e.,* while scaling down the electrode materials in to nanoscale, the large surface area will be obtained. This nanosize provides an access to the maximum number of reaction sites at the electrode–electrolyte interface as well as creating short diffusion-path length. Also it minimizes the volume expansion during Li-insertion when compared to the bulk-material counterparts, thus enhancing the specific capacities. However, this large surface area will leads to some unwanted side reactions with electrode-electrolyte interface which in turn the formation of a large amount of SEI layer that degrades the capacity. Mainly nanostructured electrode material has isolated often repeated cycling that inhibits the efficient flow of ions and electrons which leads to fast capacity fading on, especially at high current densities.[218-221]

The next approach involves hierarchical structures. Here, the secondary nanoparticles that tend to aggregate themselves in oriented manner to form hierarchical microstructures. These are potentially reducing the side reactions with the electrolyte, increases the tap density and the available nanoscale building blocks increases the kinetics of lithium ion as well as the electrical properties when compared to nanoparticles.[102, 222, 223] However, unstable SEI-film formation causes high irreversible capacities and low Coulombic efficiencies in the initial cycles.

Another approach involves the formation of composites with carbonaceous materials. The main advantages is that this prevents the side reactions with electrode/electrolyte interface and accommodate more volume strain. Among the composite, core-shell structure is the simplest strategy to enhance the electrochemical performance. Core consists of active material to involve the electrochemical reaction and shell consists of amorphous carbon which can act as protection layer to strengthen the performance of core particles. The shell has several advantages including, protecting the core from the unwanted side reactions with electrolyte, due to its flexible nature it can accommodate the volume strain and maintain the integrity, prevent the aggregation between the particles. The carbon shell has high electronic conductivity that leads to enhance the lithium ion diffusion rate. The shell thickness is also important factor that influences the electrochemical performance of core particles. So to make a proper thickness of carbon coating on the active material enhances the electrochemical performances.[4, 224] Binders are another important strategy that can overcomes the core–shell structure and graphene composite, because binders such as CMC, PAA, and sodium alginate are capable of completely covering the active material and flexibly accommodate the swelling of the electrode material.[210, 225] They also restrict the peel of active material from the current collector, facilitating the tight attachment of the active material on the current collector and enhancing the electronic conductivity. However, the binder PVDF does not.[210] The aforementioned key factors improve the electrochemical performance by accommodating the volume strain and enhancing the electronic conductivity and adhesion to the current collector. However, several problems are also persistent; stable SEI-film formation and large irreversible capacity loss mainly cause poor cycling stabilities and low Coulombic efficiencies in the first cycles, thus leading to the safety problems of using LIBs. But it can be moderately overcome by using electrolyte additives such as fluoroethylene carbonate. FEC electrolyte additives facilitate to thin SEI film formation and reducing the irreversible capacity. Therefore, it is increasing the cycle life by means of modifying the surface chemistry of the SEI film.[84, 226]

In summation, it is concluded that the electrochemical performance of the mixed-transition-metal oxides, including characteristics such as the cycling stability and rate capability, are enhanced in the following ways: synthesized mixed-metal oxides with large surface areas with porosity, composites with carbonaceous materials (core–shells and graphene), highly flexible binders (CMC, PAA, and sodium alginate), and electrolyte additives such as fluoroethylene carbonate that reduce both the irreversible capacity loss and the formation of stable SEI films. The above modifications not only make mixed-metal oxides promising high-energy-density anode materials for LIBs, but due to their multivalent states and better electronic conductivities compared to corresponding simple metal oxides, they may also be excellent candidates for bifunctional electrocatalysts and supercapacitors. Therefore, mixed-metal oxides are some of the most important forthcoming materials for the next generation of energy-storage devices.

Acknowledgements

One of the authors (RKS) is grateful to UGC (No. 41-838/2012 (SR)) for their financial support under UGC-MRP. S.Yuvaraj would like to thank UGC-BSR (No. G2/5357/2013) for providing the fellowship to carry out this work successfully.

Notes and references

1 I. Romieu, F. Menesses, S. Ruiz, J. J. Sienra, J. Huetra, M. C. White and R. A. Etzel, *American Journal of Respiratory and Critical Care Medicine,* 1996, **154,** 300-307.
2 A. Haines, R.S. Kovats, D. Campbell-Lendrum and C. Corvalan, *Public Health,* 2006, **120,** 585–596.
3 P. Knippertz, M. J. Evans, P. R. Field, A. H. Fink, C. Liousse and J. H. Marsham, *Nature Climate Change,* 2015, **5,** 815-822.
4 L. Ji, Z. Lin, M. Alcoutlabi and X. Zhang, *Energy Environ. Sci.,* 2011, **4,** 2682-2699.
5 J. W. Long, B. Dunn, D. R. Rolison and H. S. White, *Chem. Rev.,* 2004, **104,** 4463-4492.
6 M. G. Kim and J. Cho, *Adv. Funct. Mater.,* 2009, **19,** 1497-1514.
7 M. Winter and R. J. Brodd, *Chem. Rev.,* 2004, **104,** 4245-4270.

View Article Online
DOI: 10.1039/C5RA23503K

8 J. B. Goodenough and Y. Kim, *Chem. Mater.,* 2010, **22,** 587-603.
9 C. M. Hayner, X. Zhao and H. H. Kung, *Annu. Rev. Chem. Biomol. Eng.,* 2012, **3,** 445-471.
10 M. M. Thackerey, C. Wolverton and E. D. Isaacs, *Energy Environ. Sci.,* 2012, **5,** 7854-7863.
11 K. Persson, V. A. Sethuraman, L. J. Hardwick, Y. Hinuma, Y. S. Meng, A. Van der Ven, V. Srinivasan, R. Kostecki and G. Ceder, *J. Phys. Chem. Lett.,* 2010, **1,** 1176-1180.
12 J. M. Tarascon and M. Armand, *Nature,* 2001, **414,** 359-367.
13 P. Poizot, S. Laruelle, S. Grugeon, L. Dupont and J. M. Tarascon, *Nature,* 2000, **407,** 496-499.
14 J. Carbana, L. Monconduit, D. Larcher and M. R. Palacin, *Adv. Mater.,* 2010, **22,** E170-E192.
15 F. Cheng, Z. Tao, J. Liang and J. Chen, *Chem. Mater.,* 2008, **20,** 667-681.
16 A. S. Arico, P. Bruce, B. Scrosati, J. M. Tarascon and W. V. Schalkwijk, *Nat. Mater,* 2005, **4,** 366-377.
17 L. Hu, L. Wu, M. Liao, X. Hu and X. Fang, *Adv. Funct. Mater.,* 2012, **22,** 998-1004.
18 L. Qiao, X. H. Wang, L. Qiao, X. L. Sun, X. W. Li, Y. X. Zheng and D. Y. He, *Nanoscale,* 2013, **5**, 3037–3042.
19 B. Das, M. V. Reddy, S. Tripathy and B. V. R. Chowdari, *RSC Adv.,* 2014, **4**, 33883–33889.
20 C. N. Chinnasamy, A. Narayanasamy, N. Ponpandian, K. Chattopadhyay, K. Shinoda, B. Jeyadevan, K. Tohji and K. Nakatsuka, *Phys. Rev. B,* 2001, **63,** 184108-184114.
21 D. Carta, M. F. Casula, A. Falqui, D. Loche, G. Mountjoy, C. Sangregorio and A. Corrias, *J. Phys. Chem. C,* 2009, **113,** 8606-8615.
22 N. Guigue Millot, S. Begin-Colin, Y. Champion, M. H'tch, G. Le Caer and P. Perriat, *J. Sol. State Chem.,* 2003, **170,** 30-38.
23 M. Mouallem-Bahout, S. Bertrand and O. Pena, *J. Sol. State. Chem.,* 2005, **178,** 1080-1086.
24 C. M. Park, J. H. Kim, H. Kim and H. J. Sohn, *Chem. Soc. Rev.,* 2010, **39,** 3115-3141.
25 W. J. Zhang, *J. Power Sources,* 2011, **196,** 877-885.
26 T. P. Kumar, R. Ramesh, Y. Y. Lin and G. T. K. Fey, *Electrochem. Commun.,* 2004, **6,** 520-525.
27 S. Jin and C. Wang, Nano Energy, 2014, **7,** 63-71.
28 C. T. Cherian, M. Zheng, M. V. Reddy, B. V. R. Chowdari and C. H. Sow, *ACS Appl. Mater. Interfaces,* 2013, **5,** 6054-6060.
29 S. Jin, G. Yang, H. Song, H. Cui and C. Wang, ACS Appl. Mater. Interfaces, 2015, **7,** 24932-24943.
30 F. Zhang, R. Zhang, Z. Zhang, H. Wang and J. Feng, *Electrochim. Acta,* 2014, **150,** 211- 217.
31 J. Jiang, J. Luo, X. Huang, J. Liu and T. Xu, Nanoscale, 2013, **5,** 8105-8113.
32 C.W. Jung, P. Jacobs, *Mag. Res. Imag.,* 1995, **13,** 661–674.
33 J.P. Liu, Nanoscale Mag. Mater. and Appl., Springer Verlag, 2009.
34 N. Ikenaga, Y. Ohgaito, H. Matsushima, T. Suzuki, *Fuel,* 2004, **83,** 661-669.
35 Y. Yin, B. Zhang, X. Zhang, J. Xu and S. Yang, *J. Sol–Gel Sci.Technol.,* 2013, **66,** 540-543.
36 S. M. Hoque, M. Abdul Hakin, A. Mamun, S. Akhter, Md. Tanvir Hasan, D. Prasad Paul and K. Chattopadhayay, *Mater. Sci and Applications,* 2011, **2,** 1564-1571.
37 Y. Pan, Y. Zhang, X. Wei, C. Yuan, J. Yin, D. Cao and G. Wang, *Electrochim. Acta,* 2013, **109,** 89-94.
38 C. Gong, Yu-Jun Bai, Yong-Xin Qi, N. Luna and J. Feng, *Electrochim. Acta,* 2013, **90,** 119-127.
39 A. K. Rai, T. V. Thi, J. Gim and J. Kim, *Mater. Characterization.,* 2014, **95,** 259–265.
40 D. S. Mathew and R-S. Juang, *Chem. Eng. Journal,* 2007, 129, 51-65.
41 A. Shanmugavani, R. Kalai Selvan, S. Layek and C. Sanjeeviraja, *J. Magn. Magn. Mater.,* 2014, **354,** 363-371.
42 Y. Sharma, N. Sharma, G.V. Subba Rao and B.V.R. Chowdari, *Electrochim. Acta*, 2008, **53,** 2380–2385.
43 P. F. Teh, Y. Sharma, S. S. Pramana and M. Srinivasan, *J. Mater. Chem.,* 2011, **21,** 14999-15008.
44 W. Song, J. Xie, S. Liu, G. Cao and T. Zhu and X. Zhao, *New J. Chem.,* 2012, **36,** 2236– 2241.
45 J. Sui, C. Zhang, D. Hong, J. Li, Q. Cheng, Z. Li and W. Cai, *J. Mater. Chem.,* 2012, **22,** 13674-13681.
46 N. N. Wang , H. Xu, L. Chen, X. Gu, J. Yang and Y. Qian, *J. Power Sources,* 2014, **247,** 163-169.
47 Y. Deng, Q. Zhang, S. Tang, L. Zhang, S. Deng, Z. Shi and G. Chen, *Chem. Commun.,* 2011, **47,** 6828-6830.
48 Z. Xing, Z. Ju, J. Yang, H. Xu, and Y. Qian, *Nano Res.,* 2012, **5,** 477–485.
49 F. Mueller, D. Bresser, E. Paillard, M. Winter and S. Passerini, *J. Power Sources*, 2013, **236,** 87-94.
50 J. M. Won, S. H. Choi, Y. J. Hong, Y. Na Ko and Y. C. Kang, *Scientific Reports,* 2014, **4:5857,** 1-5.
51 H. Xia, Y. Qian, Y. Fu, and X. Wang, *Sol. State Sciences,* 2013, **17,** 67-71.
52 L. Yao, X. Hou, S. Hu, J. Wang, M. Li, C. Su, M. O. Tade, Z. Shao and X. Liu, J. Power Sources, 2014, **258,** 305-313.
53 D. Bresser, E. Pailard, R. Kloepsch, S. Krueger, M. Fiedler, R. Schmitz, D. Baither, M. Winter and S. Passerini, *Adv. Energy Mater.,* 2013, **3,** 513-523.
54 X. Yao, J. Kong, D. Zhou, C. Zhao, R. Zhou and X. Lu, *Carbon,* 2014, **79,** 493-499.
55 Y. Ding, Y. Yang and H. Shao, *Sol. State Ionics,* 2012, **217,** 27-33.
56 L. Luo, R. Cui, H. Qiao, K. Chen, Y. Fei, D. Li, Z. Pang, K. Liu and Q. Wei, *Electrochim. Acta,* 2014, **144,** 85–91.
57 L. Jin, Y. Qiu, H. Deng, W. Li, H. Li and S. Yang, *Electrochim. Acta,* 2011, **56,** 9127-9132.
58 M. Bomio, P. Lavela, J. Tirado, *ChemPhysChem,* 2007, **8,** 1999-2007.
59 Z. Xing, Z. Ju, J. Yang, H. Xu and Y. Qian, *Electrochim. Acta,* 2013, **102,** 51-57.
60 B. Aslibeiki, P. Kameli, H. Salamati, M. Eshraghi and T. Tahmasebi, *J. Magn. Magn. Mater.,* 2010, **322,** 2929–2934.
61 J. P. Hill, W. Jin, A. Kosaka, T. Fukushima, H. Ichihara, T. Shimomura, K. Ito, T. Hashizume, N. Ishii and T. Aida, *Science,* 2004, **304,** 1481–1483.
62 J. Dobson, *Drug Dev. Res.,* 2006, **67,** 55–60.
63 Q. A. Pankhurst, J. Connolly, S. Jones and J. Dobson, *J. Phys. D: Appl. Phys.,* 2003, **36,** 167-181.
64 Y. P. Lin and N. L. Wu, *J. Power Sources,* 2011, **196,** 851–854.
65 Z. Zhang, Y. Wang, Q. Tan, Z. Zhong and F. Su, *J. Coll. Inter. Sci.,* 2013, **398,** 185–192.
66 S.W. Oh, H.J. Bang, Y.C. Bae, Y.K. Sun, *J. Power Sources,* 2007, **173,** 502-509.
67 X.W. Lou, L.A. Archer, Z.C. Yang, *Adv. Mater.,* 2008, **20,** 3987-4019.
68 A. Latz, J. Zausch, *J. Power Sources,* 2011, **196,** 3296-3302.
69 Y. Xiao, J. Zai, L. Tao, B. Li, Q. Han, C. Yu and X. Qian, *Phys. Chem. Chem. Phys.,* 2013, **15,** 3939-3945.
70 H. Xiang, K. Zhang, G. Ji, J. Y. Lee, C. Zou, X. Chen and J. Wu, *Carbon,* 2011, **49,** 1787-1796.
71 H. Zhao, Z. Zheng, K. W. Wong, S. Wang, B. Huang, D. Li, *Electrochem. Commun.,* 2007, **9,** 2606-2610.
72 67. C. Vidal-Abarca, P. Lavela and J. L. Tirado, *J. Phys. Chem. C,* 2010, **114,** 12828-12832.

View Article Online
DOI: 10.1039/C5RA23503K

73 P. Lavela, J. L. Tirado, *J. Power Sources,* 2007, **172,** 379-387.
74 C. T. Cherian, J. Sundaramurhty, M. V. Reddy, P. S. Kumar, K. Mania, D. Pliszka, C. H. Sow, S. Ramakrishna and B. V. R. Chowdari, *Appl. Mater. Interface,* 2013, **5,** 9957-9963.
75 Y. Ding, Y. Yang and H. Shao, *J. Power Sources,* 2013, **244,** 610-613.
76 Y. Fu, Y. Wan, H. Xia and X. Wang, *J. Power sources,* 2012, **213,** 338-342.
77 G. Zhang, L. Yu, H. B. Wu, H. E. Hoster and X. W. Lou, *Adv. Mater.,* 2012, **24,** 4609-4613.
78 G. Zhou, D. W. Wang, F. Li, L. Zhang, N. Li, Z. S. Wu, L. Wen, G. Q. Lu and H. M. Cheng, *Chem. Mater.,* 2010, **22,** 5306-5313.
79 E. M. Hetdari, B. Zhang, M. H. Sohi, A. Ataie and J. K. Kim, *J. Mater. Chem. A.,* 2014, **2,** 8314-8322.
80 A. Magasinski, B. Zdyrko, I. Kovalenko, B. Hertzberg, R. Burtovyy, C. F. Huebner, T. F. Fuller, I. Luzinov and G. Yushin, *ACS Appl. Mater. Interfaces,* 2010*,* **2,** 3004-3010.
81 I. Kovalenko, B. Zdyrko, A. Magasinski, B. Hertzberg, Z. Millicev, R. Burtovyy, I. Luzinov and G. Yushin, *Science,* 2011, **334,** 75-79.
82 P. Ramesh Kumar and S. Mitra, *RSC Adv.,* 2013, **3,** 25058-25064.
83 A. M. Chockla, T. D. Bogart, C. M. Hessel, K. C. Klavetter, C. B. Mullins, and B. A. Korgel, *J. Phys. Chem. C,* 2012, **116,** 18079-18086.
84 A. M. Chockla, K. C. Klavetter, C. B. Mullins and B. A. Korgel, *Chem. Mater.* 2012, **24,** 3738-3745.
85 Y. Fu, Y. Wan, H. Xia and X. Wang, *J. Power Sources,* 2012, **213,** 338-342.
86 T. Yoon, C. Chae, Y. K. X. Zhao, H. H. Kung and J. K. Lee, *J. Mater. Chem.,* 2011, **21,** 17325-17330.
87 P. Lavela, J. L. Tirado, M. Womes and J. C. Jumas, *J. Phys. Chem. C,* 2009, **113,** 20081-20087.
88 P. R. Kumar, P. Kollu, C. Santhosh, K. E. V. Rao, D. K. Kim and A. N. Grace, *New J.Chem.,* 2014, **38,** 3654-3661.
89 84. P. Fen Teh, S. S. Pramana, Y. Sharma, Y. Wen Ko and S. Madhavi, *ACS Appl. Mater. Interfaces,* 2013, **5,** 5461-5467.
90 J. Cabana, L. Monconduit, D. Larcher and M. R. Palacin, *Adv. Mater.,* 2010, **22,** E170-E192.
91 S. Li, B. Wang, L .Liu and M. Yu, *Electrochim. Acta,* 2014, **129,** 33-39.
92 Y. Wang, D. W. Su, A. Ung, J. H. Ahn and G. X. Wang, *Nanotechnology,* 2012, **23,** 55402-55408.
93 Z. Zhang, Y. H. Wang, M. J. Zhang, Q. Q. Tan, X. Lv, Z. Y. Zhong and F. B. Su, *J. Mater. Chem. A,* 2013, **1,** 7444-7450.
94 M. Zhang, X. Yang, X. Kan, X. Wang, L. Ma and M. Jia, *Electrochim. Acta,* 2013, **112,** 727-734.
95 H. Xia, D. Zhu, Y. Fu and X. Wang, *Electrochim. Acta,* 2012, **83,** 166-174.
96 Q. Q. Xiong, J. P. Tu, S. J. Shi, X. Y. Liu, X. L. Wang and C. D. Gu, *J. Power Sources,* 2014, **256,** 153-159.
97 Y. J. Mai, X. H. Xia, R. Chen, C. D. Gu, X. L. Wang and J. P. Tu, *Electrochim. Acta,* 2012, **67,** 73-78.
98 W. Wei, J. L. Wang, L. J. Zhou, J. Yang, B. Schumann and Y. N. Nuli, *Electrochem. Commun.,* 2012, **13,** 742-745.
99 F. M. Courtel, H. Duncan, Y. A. Lebdeh and I. J. Davidson, *J. Mater. Chem.,* 2011, **21,** 10206-10218.
100 L. Zhou, H. B. Shao, J. M. Wang, L. Liu, J. Q. Zhang and C. N. Cao, *J. Mater. Chem.,* 2012, **22,** 827-829.
101 C. Yuan, H. B. Wu, Y. Xie and X. Wen (David) Lou, *Angew. Chem. Int. Ed.* 2014, **53,** 1488-1504.
102 L. Hu, H. Zhong, X. Zheng, Y. Huang, P. Zhang and Q. Chen, *Scientific Reports,* 2012, **2:986,** 1-8.
103 L. Zhou, D. Zhao and X. W. Lou, *Adv. Mater.,* 2012, **24,** 745-748.
104 G. Zhang, H. B. Wu, H. E. Hoster and X. W. (David) Lou, *Energy Environ. Sci.,* 2014, **7,** 302-305.
105 L. Wang, B. Liu, S. Ran, L. Wang, L. Gao, F. Qu, D. Chen and G. Shen, *J. Mater. Chem. A,* 2013, **1,** 2139-2143.
106 G. Yang, X. Xu, W. Yan, H. Yang and S. Ding, *Electrochim. Acta,* 2014, **137,** 462-469.
107 W. Kang, Y. Tang, W. Li, X. Yang, H. Xue, Q. Yang and C- S. Lee, *Nanoscale,* 2015, **7,** 225-231.
108 J. Maier, *Nat. Mater.,* 2005, **4,** 805-815.
109 J. Li, S. Xiong, X. Li and Y. Qian, *Nanoscale,* 2013, **5,** 2045-2054.
110 Y. Yang, Y. Zhao, L. Xiao and L. Zhang, *Electrochem. Commun.,* 2008, **10,** 1117-1120.
111 L. Xiao, Y. Yang, J. Yin, Q. Li and L. Zhang, *J. Power Sources,* 2009, **194,** 1089-1093.
112 Y. Deng, S. Tang, Q. Zhang, Z. Shi, L. Zhang, S. Zhan and G. Chen, *J. Mater. Chem.,* 2011, **21,** 11987-11995.
113 F. M. Courtel, Y. A. Lebdeh and I. J. Davidson, *Electrochim. Acta,* 2012, **71,** 123-127.
114 K. Xu, *Chem. Rev.,* 2004, **104,** 4303-4418.
115 J. G. Kim, S. H. Lee, Y. Kim and W. B. Kim, *ACS Appl. Mater. Interfaces,* 2013, **5,** 11321−11328.
116 N. Wang, X. Ma, H. Xu, L. Chen, J. Yue, F. Niu, J. Yang and Y. Qian, *Nano Energy,* 2014, ***6,*** *193-199.*
117 Y. Liu, J. Bai, X. Ma, J. Li and S. Xiong, *J. Mater. Chem. A.,* 2014, **2,** 14236-14244.
118 Z. Bai, N. Fan, C. Sun, Z. Ju, C. Guo, J. Yang and Y. Qian, *Nanoscale,* 2013, **5,** 2442-2447.
119 P. Xiong, B. Liu, V. Teran, Y. Zhao, L. Peng, X. Wang and G. Yu, *ACS NANO,* 2014, **8,** 8610-8616.
120 L. Zhou, H. B. Wu, T. Zhu and X. W. (David) Lou, *J. Mater. Chem.,* 2012, **22,** 827-829.
121 S. Vijayanand, P. A. Joy, H. S. Potdar, D. Patil and P. Patil, *Sensors and Actuators B* 2011, **152,** 121-129.
122 M. Prabu, K. Ketpang and S. Shanmugam, *Nanoscale,* 2014, **6,** 3173-3181.
123 Q. Lu, Y. Chen, W. Li, J. G. Chen, J. Q. Xiao and F. Jiao, J. Mater. Chem. A, 2013, **1,** 2331-2336.
124 Y. Sharma, N. Sharma, G. V. Subba Rao and B. V. R. Chowdari, *J. Power Sources,* 2007, **173,** 495-501.
125 Y. Sharma, N. Sharma, G. V. Subba Rao and B. V. R. Chowdari, *Solid State Ionics,* 2008, **179,** 587-597.
126S. Sun, Z. Wen, J. Jin, Y. Cui and y. Lu, *Micro. Meso. Mater.* 2013, **169,** 242-247.
127 B. Y. Sharma, N. Sharma, G. V. Subba Rao and B. V. R. Chowdari, *Adv. Func. Mater,* 2007, **17,** 2855-2861.
128 W. Luo, X. Hu, Y. sun and Y. Huang, *J. Mater. Chem.,* 2012, 22, 8916-8921.
129 B. Liu, J. Zhang, X. Wang, G. Chen, D. Chen, C. Zhou and G. Shen, *Nano Lett.,* 2012, **12,** 3005-3011.
130 Q. Xie, F. Li, H. Guo, L. Wang, Y. Chen, G. Yue and D. L. Peng, *ACS Appl. Mater. Interfaces,* 2013, **5,** 5508-5517.
131 H. Long, T. Shi, S. Jiang, S. Xi, R. Chen, S. Liu, G. Liao and Z. Tang, *J. Mater. Chem. A,* 2014, **2,** 3741-3748.
132 L. Hu, B. Qu, C. Li, Y. Chen, L. Mei, D. Lei, L. Chen, Q. Li and T. Wang, *J. Mater. Chem. A,* 2013, **1,** 5596-5602.
133 J. Li, J. Wang, D. Wexler, D. Shi, J. Liang, H. Liu, S. Xiong and Y. Qian, *J. Mater. Chem. A,* 2013, **1,** 15292-15299.
134 B. Qu, L. Hu, Q. Li, Y. Wang, L. Chen and T. Wang, *ACS Appl. Mater. Interfaces,* 2014, **6,** 731-736.
135 G. Zhou, D. W. Wang, F. Li, L. Zhang, N. Li, Z. S. Wu, L. Wen, G. Q. Lu and H. M. Cheng, *Chem. Mater.,* 2010, **22,** 5306-5313.
136 L. Li, Y. Q. Zhang, X. Y. Liu, S. J. Shi, X. Y. Zhao, X. Ge, G. F. Cai, C. D. Gu, X. L. Wang and J. P. Tu, *Electrochim. Acta,* 2014, 116, 467-474.
137 S. G. Mohamed, T-F. Hung, C-J. Chen, C. K. Chen, S-F. Hu and R-S. Liu, *RSC Adv.,* 2014, **4,** 17230-17235.
138 J. Xu, L. He, W. Xu, H. Tang, H. Liu, T. Han, C. Zhang, Y. Zhang, *Electrochim. Acta,* 2014, **145,** 185-192.

View Article Online
DOI: 10.1039/C5RA23503K

139 J. Shen, X. Li, N. Li and M. Ye, *Electrochim. Acta,* 2014, **141,** 126-133.
140 X. Hou, X. Wang, B. Liu, Q. Wang, T. Luo, D. Chen and G. Shen, *Nanoscale,* 2014, **6,** 8858-8864.
141 C. Fu, G. Li, D. Luo, X. Huang, J. Zheng and L. Li, *ACS Appl. Mater. Interfaces,* 2014, 6, 2439-2449.
142 J. Li, S. Xiong, X. Li and Y. Qian, *J. Mater. Chem.,* 2012, **22,** 23254-23259.
143 L. Shen, L. Yu, X-Y. Yu, X. Zhang and X. W (David) Lou, *Angew Chem.,* 2014, **126,** 1-6.
144 J. Li, S. Xiong, Y. Liu, Z. Ju and Y. Qian, *ACS Appl. Mater. Interfaces,* 2013, **5,** 981-988.
145 H. S. Jadhav, R. S. Kalubarme, C-N. Park, J. Kim and C-J. Park, *Nanoscale,* 2014, **6,** 10071-10076.
146 M. Alcantara, M. Jaraba, P. Lavela and J. L. Tirado, *Chem. Mater.,* 2002, **14,** 2847-2848.
147 A. K. Rai, T. V. Thi, B. J. Paul and J. Kim, *Electrochim. Acta,* 2014, **146,** 577-584.
148 X. Song, Q. Ru, Y. Mo, S. Hu and B. An, *J. Alloys. Compds.,* 2014, 606, 219-225.
149 X. Song, Q. Ru, B. Zhang, S. Hu and B. An, J. Alloys. Compds., 2014, **585,** 518-522.
150 N. Du, Y. Xu, H. Zhang, J. Yu, C. Zhai and D. Yang, *Inorg. Chem.,* 2011, **50,** 3320-3324.
151 R. Wu, X. Qian, K. Zhou, J. Wei, J. Lou and P. M. Ajayan, *ACS NANO,* 2014, **8,** 6297-6303.
152 S. H. Choi and Y. C. Kang, *ChemSusChem,* 2013, **6,** 2111-2116.
153 S. G. Mohamed, T-F. Hung, C-J. Chen, C. K. Chen, S-F. Hu, R-S. Liu, K-C. Wang, X-K. Xing, H-M. Liu, A-S. Liu, M-H. Hsieh and B-J. Lee, *RSC Adv.,* 2013, 3, 20143-20149.
154 A. K. Mondal, D. Su, S. Chen, K. Kretschmer, X. Xie, H-J. Ahn and G. Wang, *ChemPhysChem,* 2015, **16,** 169-175.
155 A. K. Mondal. D. Su, S. Chen, X. Xie and G. Wang, *ACS Appl. Mater. Interfaces,* 2014, **6,** 14827-14835.
156 F. Zheng, D. Zhu and Q. Chen, *ACS Appl. Mater. Interfaces,* 2014, **6,** 9256-9264.
157 X. Yao, C. Zhao, J. Kong, D. Zhou and X. Lu, *RSC Adv.,* 2014, **4,** 37928-37933.
158 H. Guo, L. Liu, T. Li, W. Chen, J. Liu, Y. Guo and Y. Guo, *Nanoscale,* 2014, **6,** 5491-5497.
159 S. G. Mohamed, C-J. Chen, C. K. Chen, S-F. Hu and R-S. Liu, *ACS Appl. Mater. Interfaces,* 2014, **6,** 22701-22708.
160 X. Shen, D. Mu, S. Chen, B. Wu and F. Wu, *ACS Appl. Mater. Interfaces,* 2013, **5,** 3118-3125.
161 Y. M. Lin, K. C. Klavetter, A. Heller and C. B. Mullins, *J. Phys. Chem. Lett.,* 2013, **4,** 999-1004.
162 J. K. Feng, M. O. Lai and L. Lu, *Electrochem. Commun.,* 2011, **13,** 287-289.
163 F. Zou, X. Hu, L. Qie, Y. Jiang, X. Xiong, Y. Qiao and Y. Huang, *Nanoscale,* 2014, **6,** 924-930.
164 W. W. Li, X. F. Wang, B. Liu, S. J. Luo, Z. Liu, X. J. Hou, Q. Y. Xiang, D. Chen and G. Z. Shen, *Chem-Eur. J.,* 2013, **19,** 8650-8656.
165 W. Li, Y. X. Yin, S. Xin, W. G. Song and Y. G. Guo, *Energy Environ. Sci.,* 2012, **5,** 8007-8013.
166 R. Yi, J. K. Feng, D. P. Lv, M. L. Gordin, S. R. Chen, D. W. Choi and D. H. Wang, *Nano Energy,* 2013, **2,** 498-504.
167 F. Zou, X. Hu, Y. Sun, W. Luo, F. Xia, L. Qie, Y. Jiang and Y. Huang, *Chem-Eur. J.,* 2013, **19,** 6027-6033.
168 R. Wang, S. Wu, Y. Lv and Z. Lin, Langmuir, 2014, **30,** 8215-8220.
169 C. H. Kim, Y. S. Jung, K. T. Lee, J. H. Ku, S. M. Oh, *Electrochim. Acta,* 2009, **54,** 4371-4377.
170 Y. Feng, X. Li, Z. Shao and H. Wang, *J. Mater. Chem. A,* 2015, **3,** 15274-15279.
171 P. A. Connor, J. T. S. Irvine, *J. Power Sources,* 2001, **97-98,** 223-225.
172 P. A. Connor, J. T. S. Irvin, Electrochim. Acta, 2002, **47,** 2885-2892.
173 R. Alcantara, G. F. Ortiz, P. Lavela, J. L. Tirado, *Electrochem. Commun.,* 2006, 8, 731-736.
174 S. Lei, K. Tang, C. Chen, Y. Jin and L. Zhou, Mater. Res. Bull., 2009, **44,** 393-397.
175 X. J. Zhu, L. M. Geng, F. Q. Zhang, Y. X. Liu and L. B. Cheng, J. Power Sources, 2009, **189,** 828-831.
176 G. Wang, X. P. Gao and P. W. Shen, *J. Power Sources,* 2009, **192,** 719-723.
177 Y. Qi, N. Du, H. Zhang, P. Wu and D. Yang, *J. Power Sources,* 2011, **196,** 10234-10239.
178 S. Yuvaraj, S. Amaresh, Y.S. Lee and R. Kalai Selvan, *RSC Adv.,* 2014, **4,** 6407-6416.
179 G. Wang, Z. Y. Liu and P. Liu, *Electrochim. Acta,* 2011, **56,** 9515-9519.
180 J. Zhang, J. Liang, Y. Zhu, D. Wei, L. Fan and Y. Qian, *J. Mater. Chem. A,* 2014, **2,** 2728-2734.
181 J. M. Schnorr, T. M. Swagar, *Chem. Mater.,* 2011, **23,** 646-657.
182 C. Masarapu, V. Subramanian, H. Zhu, B. Wei, J. Feng, M. Zhang, W. Qian and F. Wei, *Adv. Mater.,* 2010, **22,** 3723-3728.
183F. F. Cao, Y. G. Guo, S. F. Zheng, X. L. Wu, L. Y. Jiang, R. R. Bi, L. J. Wan and J. Maier, *Chem. Mater.,* 2010, **22,** 1908-1914.
184 S. F. Feng, J. S. Hu, L. S. Zhong, W. G. Song. L. J. Wan and Y. G. Guo, *Chem. Mater.,* 2008, **20,** 3617-3622.
185 H. C. Liu and S. K. Yen, *J. Power Sources,* 2007, **166,** 478-484.
186 X. Hou, Q. Cheng, Y. Bai and W. F. Zhang, *Sol. State Ionics,* 2010, **181,** 631-634.
187 N. Feng, S. Peng, X. Sun, L. Qiao, X. Li, P. Wang, D. Hu and D. He, Mater. Lett., 2012, **76,** 66-68.
188 J. Yu, G. Choi, *Sens. Actuators B,* 2001, **72,** 141-148.
189 B. Tan, E. Toman, Y. Li and Y. Wu, *J. Am. Chem. Soc.,* 2007, **129,** 4162-4163.
190Y. Lin, S. Lin, M. Luo and J. Liu, *Mater. Lett.,* 2009, **63,** 1169-71.
191 J. W. Lee and C. H. Lee, *J. Supercritical Fluids,* 2010, **55,** 252-258.
192 F. Belliard, P. A. Connor and J. T. S. Irvine, *Sol. State Ionics,* 2000, **135,** 163-167.
193 A. Rong, X. P. Gao, G. R. Li, T. Y. Yan, H. Y. Zhu, J. Q. Qu and D. Y. Song, *J. Phys. Chem. B,* 2006, **110,** 14754-14760.
194 W. S. Yuan, Y. W. Tian and G. Q. Liu, *J. Alloys. Compd.,* 2010, **506,** 683-687.
195 K. Kim, A. Annamalai, S. H. Park, T. H. Kwon, M. W. Pyeon and M, J. Lee, *Electrochim. Acta,* 2012, **76,** 192-200.
196 Y. Zhao, Y. Huang, Q. Wang, K. Wang, M. Zong, L. Wang and X. Sun, Ceramics International, 2014, **40,** 2275-2280.
197 R. Zhang, Y. He and L. Xu, *J. Mater. Chem. A,* 2014, **2,** 17979-17985.
198 H. Huang, Y. Huang, M. Wang, X. Chen, Y. Zhao, K. Wang and H. Wu, *Electrochim. Acta,* 2014, **147,** 201-208.
199 W. Song, J. Xie, W. Hu, S. Liu, G. Cao, T. Zhu and X. Zhao, *J. Power Sources,* 2013, **229,** 6-11.
200 Y. Zhao, Y. Huang, X. Sun, H. Huang, K. Wang, M. Zong and Q. Wang, *Electrochim. Acta,* 2014, **120,** 128-132.
201 K. Wang, Y. Huang, Y. Shen, L. Xue, H. Huang, H. Wu and Y. Wang, *Cer. Inter.,* 2014, 40, 15183-15190.
202 X. Zheng, Y. Li, Y. Xu, Z. Hong and M. Wei, *CrystEngComm,* 2012, **14,** 2112-2116.
203 K. Wang, Y. Huang, T. Han, Y. Zhao, H. Huang and L. Xue, Cer. Inter., 2014, **40,** 2359-2364.
204 Y. Zhao, Y. Huang, L. Xue, X. Sun, Q. Wang, W. Zhang, K. Wang and M. Zong, *Polymer Testing,* 2013, **32,** 1582-1587.

View Article Online
DOI: 10.1039/C5RA23503K

205 G. F. Ma, H. Peng, J. J. Mu, H. H. Huang, X. Z. Zhou and Z. Q. Lei, *J. Power Sources,* 2013, **229,** 72-78.
206 S. Zhang, M. Lu, Y. Li, F. Sun, J. Yang and S. Wang, *Mater. Lett.,* 2013, **100,** 89-92.
207 F. Mueller, D. Bresser, N. Minderjahn, J. Kalhoff, S. Menne, S. Krueger, M. Winter and S. Passerini, *Dalton Trans.,* 2014, **43,** 15013-15021.
208 S. Yuvaraj, K. Karthikeyan, L. Vasylechko and R. Kalai Selvan, *Electrochim. Acta,* 2015, **158,** 446-456.
209 S. Zhang, L. Ren and S. Peng, *CrystEngComm,* 2014, **16,** 6195-6202.
210 S-L. Chou, Y. Pan, J-Z. Wang, H-K. Liu, and S-X. Dou, Phys. Chem. Chem. Phys., 2014, **16,** 20347-20359.
211 S. S. Zhang, K. Xu and T. R. Jow, *J. Power Spurces,* 2004, **138,** 226.
212 J. H. Lee, S. Lee, U. Paik and Y. M. Choi, *J. Power Sources,* 2005, **147,** 249.
213 R. Zhang, X. Yang, D. Zhang, H. Qiu, Q. Fu, H. Na, Z. Guo, F. Du, G. Chen and Y. Wei, *J. Power Sources,* 2015, **285,** 227-234.
214 J. S. Bridel, T. Azais, M. Morcrette, J. M. Tarascon and D. Larcher, *Chem. Mater.,* 2010, **22,** 1229.
215 D. Mazouzi, B. Lestriez, L. Roue, D. Guyomard, *Electrochem. Solid-State Lett.,* 2009, **12,** A215.
216 U. Kumar Sen and S. Mitra, *ACS Appl. Mater. Interface,s* 2013, **5,** 1240-1247.
217 S. Mitra, P. S. Veluri, A. Chakraborthy and R. K. Petla, *ChemElectroChem,* 2014, 1, 1068-1074.
218 H. B. Wu, J. S. Chen, H. H. Hng and X. Wen (David) Lou, *Nanoscale,* 2012, **4,** 2526-2542.
219 J. Xiao, J. Zheng, X. Li, Y. Shao and J-G. Zhang, *Nanotechnology,* 2013, **24,** 424004-424011.
220 H. Zhang, X. Yu and P. Braun, *Nature Nanotechnol.* 2011, **6,** 277-281.
221 H. Li, L. Shen, G. Pang, S. Fang, H. Luo, K. Yang and X. Zhang, *Nanoscale,* 2015,**7**, 619-624.
222 D. Li, C. Feng, H. K. Liu and Z. Guo, *Scientific Reports,* 5: 11326.
223 J. Xiao, *Nano Lett.,* 2011, **11**, 5071–5079.
224 S. Yuvaraj, W. J. Lee, C. W. Lee and R. Kalai Selvan, *RSC Adv.,* 2015, **5,** 67210-67219.
225 L. Su, Y. Jing and Z. Zhou, *Nanoscale,* 2011, **3,** 3967-3983.
226V. Etacher, O. Haik, Y. Goffer, G. A. Roberts, I. C. Stefen, R. Fasching, D. Aurbach, *Langmuir,* 2012, **28,** 965-976.
227 L. Lin and Q. Pan, *J. Mater. Chem. A,* 2015, **3,** 17247-1729.
228 B. Wang, S. Li, B. Li, J. Liu and M. Yu, *New J. Chem.,* 2015, **39,** 1725-1733.
229 R. M. Thankachan, M. M. Rahman, I. Sultana, A. M. Glushenkov, S. Thomas, N. Kalarikkal and Y. Chen, *J. Power Sources,* 2015, **282,** 462-470.
230 W. Yao, J. Xu, W. J. Luo, Q. Shi and Q. Zhang, *ACS Sustainable Chem. Eng.,* 2015, **3,** 2170-2177**.**
231 Y. Mo, Q. Ru, X. Song, S. Hu, L. Guo and X. Chen, *Electrocchim. Acta,* 2015, **176,** 575-585.
232 L. Peng, H. Zhang, Y. Bai, J. Yang and Y. Wang*, J. Mater. Chem. A,* 2015, **3,** 22094-22101.
233 Q. Li, X. Miao, C. Wang and L. Yin, *J. Mater. Chem. A,* 2015, **3,** 21328-21336.
234 W. Chen, L. Lu, S. Maloney, Y. Yang and W. Wang, *Phys. Chem. Chem. Phys.,* 2015, **17,** 5109-5114.
235 W. Chen, S. Maloney and W. Wang, *Electrochim. Acta,2015, 176, 96-102.*

View Article Online
DOI: 10.1039/C5RA23503K

Table 1. Comparison of lead–acid, Ni–Cd, Ni–metal hydride, and Li-ion batteries.

Specifications	Lead-Acid	Ni-Cd	Ni-MH	Li-ion batteries		
				$LiCoO_2$	$LiMn_2O_4$	$LiFePO_4$
Cell Voltage	2.1V	1.2V	1.2V	3.7V	3.7V	3.3V
Energy Density (Wh Kg^{-1})	30-50	45-80	60-120	150-190	100-135	90-120
Power Density (W Kg^{-1})	180	150	250-1000	1800	1200-1400	1400
Cycle life (cycles)	400	500	500	>500	>500	>2000
Energy Efficiency (%)	60	70	90	75	90	95
Self-discharge (%) per month	20	30	35	10	10	8
Memory Effect	No	Yes	Little	No	No	No

View Article Online
DOI: 10.1039/C5RA23503K

Table 2. A Summary of recent electrochemical studies on Zn_2SnO_4 based anodes for LIBs.

Sample	Experimental methods	Specific capacity	Rate capability	Ref
$ZnFe_2O_4$	Combustion synthesis	615 mAh g^{-1} at 60 mA g^{-1}, 50 cycles	-	(42)
$ZnFe_2O_4$ nanofibers	Electrospinning technique	733 mAh g^{-1} at 60mA g^{-1}, 30 cycles	400 mAh g^{-1} at 800 mA g^{-1}	(43)
$ZnFe_2O_4$/graphene hybrid	Solvothermal route	600 mAh g^{-1} at 200mA g^{-1}, 90 cycles	450 mAh g^{-1} at 800 mA g^{-1}	(44)
MWCNT–$ZnFe_2O_4$ nanocomposites	Solvothermal route	1152 mAh g^{-1} at 60 mA g^{-1}, 50 cycles	580 mAh g^{-1} at 600 mA g^{-1}	(45)
$ZnFe_2O_4$- nanorod	Template assisted method at 700˚C	888 mAh g^{-1} at 150 mA g^{-1}, 80 cycles	625 mAh g^{-1} at 1000 mA g^{-1}	(46)
$ZnFe_2O_4$/C hollow sphere	Solvothermal route	625 mAh g^{-1} at 500 mA g^{-1}, 30 cycles	450 mAh g^{-1} at 700 mA g^{-1}	(47)
$ZnFe_2O_4$ Nano-Octahedrons	Hydrothermal synthesis	910 mAh g^{-1} at 60 mA g^{-1}, 80 cycles	730 mAh g^{-1} at 1000 mA g^{-1}	(48)
$ZnFe_2O_4$ –Carbon conductive network	Carbonothermal method using sucrose	1100 mAh g^{-1} at 50 mA g^{-1}, 60 cycles	-	(49)
Yolk-shell $ZnFe_2O_4$	Spray-drying process	862 mAh g^{-1} at 500 mA g^{-1}, 200 cycles	-	(50)
$ZnFe_2O_4$/Graphene nanoparticles	Hydrothermal method	956 mAh g^{-1} at 100 mA g^{-1}, 50 cycles	600 mAh g^{-1} at 1000 mA g^{-1}	(51)
Mesoporous $ZnFe_2O_4$/C composite microspheres	Hydrothermal method using sucrose	1150 mAh g^{-1} at 50 mA g^{-1}, 100 cycles	600 mAh g^{-1} at 1100 mA g^{-1}	(52)
Carbon coated $ZnFe_2O_4$ nanoparticles	Carbonothermal method using sucrose	1300 mAh g^{-1} at 40 mA g^{-1}, 100 cycles	525 mAh g^{-1} at 3890 mA g^{-1}	(53)
Mesoporous $ZnFe_2O_4$/Graphene composite	Ambient pressure method	1259 mAh g^{-1} at 100 mA g^{-1}, 30 cycles	726 mAh g^{-1} at 2000 mA g^{-1}	(54)
$ZnFe_2O_4$@C/graphene nanocomposite	Hydrothermal method followed by carbon coating and graphene composite process	705 mAh g^{-1} at 232 mA g^{-1}, 180 cycles	403 mAh g^{-1} at 5C	(227)
$ZnFe_2O_4$/graphene hybrid films	One-step lectrophoretic deposition subsequent thermal annealing	881 mAh g^{-1} at 200 mA g^{-1}, 200 cycles	510 mAh g^{-1} at 3200 mA g^{-1}	(228)
$ZnFe_2O_4$-C nanocomposite	Sol-gel followed by ball milling technique	681 mAh g^{-1} at 0.1C, 100 cycles	469 mAh g^{-1} at 4C	(229)

View Article Online
DOI: 10.1039/C5RA23503K

Table 3.A summary on recent Electrochemical performance of MMn_2O_4 (M= Co, Zn) anodes for LIBs.

Sample	Experimental methods	Reversible capacity	Rate performance	Ref
$CoMn_2O_4$ hierarchical microspheres	Solvothermal method	894 mAh g^{-1} at 100 mA g^{-1}, 65 cycles	344 mAh g^{-1} at 7200 mA g^{-1}	(102)
Double-shelled $CoMn_2O_4$ hollow microcubes	Co-precipitation and annealing process	624 mAh g^{-1} at 200 mA g^{-1}, 50 cycles	406 mAh g^{-1} at 800 mA g^{-1}	(103)
CNF@$CoMn_2O_4$ nanocables	Polyol method and subsequent annealing treatment	870 mAh g^{-1} at 200 mA g^{-1}, 150 cycles	390 mAh g^{-1} at 2400 mA g^{-1}	(104)
$CoMn_2O_4$ nanorods	Hydrothermal and subsequent annealing process	520 mAh g^{-1} at 200 mA g^{-1}, 50 cycles	450 mAh g^{-1} at 800 mA g^{-1}	(105)
$CoMn_2O_4$ nanofibers	Electrospinning technique	526 mAh g^{-1} at 400mA g^{-1}, 90 cycles	463 mAh g^{-1} at 800 mA g^{-1}	(106)
$CoMn_2O_4$ quasi-hollow spheres	Solvothermal route	706 mAh g^{-1} at 200 mA g^{-1}, 25 cycles	450 mAh g^{-1} at 400 mA g^{-1}	(109)
Nanocrystalline-$ZnMn_2O_4$	Polymer-pyrolysis route	569 mAh g^{-1} at 100 mA g^{-1}, 50 cycles	-	(110)
Flower-like $ZnMn_2O_4$	Solvothermal process	626 mAh g^{-1} at 100 mA g^{-1}, 50 cycles	-	(111)
Nano-$ZnMn_2O_4$	Single precursor route	640 mAh g^{-1} at 100 mA g^{-1}, 50 cycles	405 mAh g^{-1} at 400 mA g^{-1}	(112)
$ZnMn_2O_4$ nanoparticles	Hydrothermal method	430 mAh g^{-1} at 78 mA g^{-1}, 100 cycles	120 mAh g^{-1} at 784 mA g^{-1}	(113)
$ZnMn_2O_4$	Co-precipitation route	800 mAh g^{-1} at 78 mA g^{-1}, 100 cycles	230 mAh g^{-1} at 1560 mA g^{-1}	(99)
$ZnMn_2O_4$-Tubular arrays	Template route	784 mAh g^{-1} at 100 mA g^{-1}, 100 cycles	363 mAh g^{-1} at 1600 mA g^{-1}	(115)
Porous $ZnMn_2O_4$ microsphere	Solvothermal method	800 mAh g^{-1} at 500 mA g^{-1}, 300 cycles	395 mAh g^{-1} at 2000 mA g^{-1}	(116)
Quasi-mesocrystal $ZnMn_2O_4$ twin microsphere	Solvothermal method	860 mAh g^{-1} at 500 mA g^{-1}, 130 cycles	329 mAh g^{-1} at 5000 mA g^{-1}	(117)
Loaf-like $ZnMn_2O_4$ nanorods	Solid state reaction	517 mAh g^{-1} at 500 mA g^{-1}, 100 cycles	457 mAh g^{-1} at 1000 mA g^{-1}	(118)
2-D hybrid $ZnMn_2O_4$-graphene nanosheet	Reflux method	800 mAh g^{-1} at 500 mA g^{-1}, 100 cycles	650 mAh g^{-1} at 2000 mA g^{-1}	(119)
$ZnMn_2O_4$ hollow microsphere	Co-precipitation and annealing method	607 mAh g^{-1} at 400 mA g^{-1}, 100 cycles	361 mAh g^{-1} at 1600 mA g^{-1}	(120)
MWCNT/$ZnMn_2O_4$	Polyol method subsequent thermal annealing process	847 mAh g^{-1} at 400 mA g^{-1}, 100 cycles	527 mAh g^{-1} at 1600 mA g^{-1}	(230)

Table 4. A summary on recent studies of spinel cobaltites (MCo_2O_4: M= Zn, Mn, Ni and Fe) for LIB anode materials.

View Article Online
DOI: 10.1039/C5RA23503K

Sample	Experimental method	Reversible capacity	Rate performance	Ref
Nanophase $ZnCo_2O_4$	Combustion method	894 mAh g^{-1} at 60 mA g^{-1}, 60 cycles	400 mAh g^{-1} at 0.7 C	(127)
Porous $ZnCo_2O_4$ nanotubes	Electrospinning technique	1454 mAh g^{-1} at 100 mA g^{-1}, 30 cycles	794 mAh g^{-1} at 2000 mA g^{-1}	(128)
$ZnCo_2O_4$ nanowires /Carbon cloth	Hydrothermal method	1278 mAh g^{-1} at 200mA g^{-1}, 100 cycles	605 mAh g^{-1} at 5C	(129)
Double –Shelled $ZnCo_2O_4$ hollow microspheres	citrate route followed by calcination	1019 mAh g^{-1} at 90 mA g^{-1}, 120 cycles	570 mAh g^{-1} at 5C	(130)
Hierarchical $ZnCo_2O_4$/Ni current collector	Hydrothermal process	1050 mAh g^{-1} at 100 mA g^{-1}, 60 cycles	240 mAh g^{-1} at 2778 mA g^{-1}	(131)
Mesoporous $ZnCo_2O_4$ microspheres	Solvothermal route	721 mAh g^{-1} at 100 mA g^{-1}, 80 cycles	382 mAh g^{-1} at 5000 mA g^{-1}	(132)
Yolk-shelled $ZnCo_2O_4$ microsphere	Refluxing route	949 mAh g^{-1} at 200 mA g^{-1}, 100 cycles	331 mAh g^{-1} at 1000 mA g^{-1}	(133)
Hierarchical $ZnCo_2O_4$ Nanostructure on Ni foam	Hydrothermal process	1122 mAh g^{-1} at 0.5 A g^{-1}, 50 cycles	542 mAh g^{-1} at 2000 mA g^{-1}	(134)
$ZnCo_2O_4$/graphene nanosheets	Auto-combustion method	755 mAh g^{-1} at 0.1C, 70 cycles	302 mAh g^{-1} at 4.5C	(147)
Fiber bundle structure $ZnCo_2O_4$	Co-precipitation method	1026 mAh g^{-1} at 100 mA g^{-1}, 100 cycles	606 mAh g^{-1} at 2000 mA g^{-1}	(148)
Flake-by-flake $ZnCo_2O_4$	Co-precipitation	1275 mAh g^{-1} at 100 mA g^{-1}, 100 cycles	730 mAh g^{-1} at 3000 mA g^{-1}	(149)
Porous $ZnCo_2O_4$ Nanowires	Sacrificial Template route	1197 mAh g^{-1} at 100 mA g^{-1}, 20 cycles	-	(150)
Porous $Zn_xCo_{3-x}O_4$ hollow polyhedra	ZIFs templating approach	990 mAh g^{-1} at 100 mA g^{-1}, 50 cycles	575 mAh g^{-1} at 10C	(151)
Yolk-Shell $ZnCo_2O_4$	Gas-phase reaction	753 mAh g^{-1} at 3000 mA g^{-1}, 200 cycles	-	(152)
Flower-like $ZnCo_2O_4$ nanowires	Hydrothermal method	900 mAh g^{-1} at 200 mA g^{-1}, 50 cycles	347 mAh g^{-1} at 800 mA g^{-1}	(153)
1D-$MnCo_2O_4$ nanowire	Hydrothermal	895 mAh g^{-1} at 100 mA g^{-1}, 50 cycles	345 mAh g^{-1} at 1000 mA g^{-1}	(136)
Hierarchical $MnCo_2O_4$ nanowire	Hydrothermal/calcination approach	1038 mAh g^{-1} at 200 mA g^{-1}, 45 cycles	388 mAh g^{-1} at 1600 mA g^{-1}	(137)
Hierarchical $MnCo_2O_4$ nanosheets/carbon cloth	Hydrothermal method	3 mAh cm^{-2} at 800 μA cm^{-2}, 60 cycles	2 mAh cm^{-2} at 1600 μA cm^{-2}	(140)
$MnCo_2O_4$ microsphere	solvothermal route	722 mAh g^{-1} at 200 mA g^{-1}, 25 cycles	320 mAh g^{-1} at 900 mA g^{-1}	(141)
$Mn_{1.5}Co_{1.5}O_4$ core-shell microsphere	Urea assisted solvothermal route	618 mAh g^{-1} at 400 mA g^{-1}, 300 cycles	455 mAh g^{-1} at 800 mA g^{-1}	(142)
Multiporous $MnCo_2O_4$	Solvothermal route	755 mAh g^{-1} at 200 mA g^{-1}, 25 cycles	610 mAh g^{-1} at 400 mA g^{-1}	(109)
Porous $NiCo_2O_4$ microflowers	Solvothermal route	952 mAh g^{-1} at 100 mA g^{-1}, 60 cycles	720 mAh g^{-1} at 500 mA g^{-1}	(138)
Uniform $NiCo_2O_4$ Hollow Spheres	Solvothermal route	885 mAh g^{-1} at 150 mA g^{-1}, 50 cycles	533 mAh g^{-1} at 2000 mA g^{-1}	(143)
$NiCo_2O_4$ Mesoporous Microspheres	Thermal decomposition	1198 mAh g^{-1} at 200 mA g^{-1}, 30 cycles	705 mAh g^{-1} at 800 mA g^{-1}	(144)
Mesoporous $NiCo_2O_4$	Co-precipitation	1000 mAh g^{-1} at 0.5 C, 400 cycles	718 mAh g^{-1} at 10 C	(145)
Mesopoprous $NiCo_2O_4$ Nanosheets	Microwave method	767 mAh g^{-1} at 100 mA g^{-1}, 50 cycles	487 mAh g^{-1} at 1000 mA g^{-1}	(154)
Porous $NiCo_2O_4$ Nanobelts	Hydrothermal technique	981 mAh g^{-1} at 500 mA g^{-1}, 100 cycles	1062 mAh g^{-1} at 2000 mA g^{-1}	(155)
Porous $Ni_xCo_{3-x}O_4$ Nanosheets	Thermal decomposition	844 mAh g^{-1} at 500 mA g^{-1}, 200 cycles	293 mAh g^{-1} at 1600 mA g^{-1}	(156)
Hollow $NiCo_2O_4$ nanospheres	Template method	1346 mAh g^{-1} at 100 mA g^{-1}, 20 cycles	695 mAh g^{-1} at 2000 mA g^{-1}	(157)
$NiCo_2O_4$ nanocubes	Etching and precipitation	1160 mAh g^{-1} at 200 mA g^{-1}, 200 cycles	750 mAh g^{-1} at 1000 mA g^{-1}	(158)
Porous $NiCo_2O_4$@C nanocomposite	Hydrothermal	1389 mAh g^{-1} at 0.55 C, 180 cycles	625 mAh g^{-1} at 4.4 C	(231)
Peapod-like $NiCo_2O_4$-C nanorods	Hydrothermal	1183 mAh g^{-1} at 100 mA g^{-1}, 200 cycles	664 mAh g^{-1} at 2000 mA g^{-1}	(232)
$FeCo_2O_4$ Nanoflakes	Hydrothermal	905 mAh g^{-1} at 200 mA g^{-1},170 cycles	1222 mAh g^{-1} at 800 mA g^{-1}	(159)

View Article Online
DOI: 10.1039/C5RA23503K

Table 5. A summary on electrochemical performance of $M_2M'O_4$ (M= Zn and Co, M'= Sn and Ge) based anodes for LIBs.

Sample	Experimental methods	Reversible capacity	Rate performance	Ref
Zn_2SnO_4 Nanowires	Vapour transport method	660 mAh g^{-1} at 120 mA g^{-1}, 50 cycles	-	(28)
Zn_2SnO_4	Hydrothermal method	644 mAh g^{-1} at 50 mA g^{-1}, 20 cycles	-	(175)
Zn_2SnO_4 cubic crystals	Solid state reaction	689 mAh g^{-1} at 50 mA g^{-1}, 50 cycles	-	(186)
Zn_2SnO_4 cubes	Hydrothermal method	775 mAh g^{-1} at 50 mA g^{-1}, 20 cycles	-	(187)
Zn_2SnO_4	Supercritical water	856 mAh g^{-1} at 0.75 mA/cm^2, 50 cycles	-	(191)
Cube shaped-Zn_2SnO_4 particles	Hydrothermal method	580 mAh g^{-1} at 100 mA g^{-1}, 50 cycles	-	(193)
Zn_2SnO_4/C composite	Hydrothermal method	563 mAh g^{-1} at 60 mA g^{-1}, 40 cycles	-	(194)
Crystalline Zn_2SnO_4 nanoparticles	Hydrothermal method	521 mAh g^{-1} at 50 mA g^{-1}, 40 cycles	-	(195)
Hollow Zn_2SnO_4@N-C composite	Co-precipitation method followed by calcination	616 mAh g^{-1} at 300 mA g^{-1}, 45 cycles	354 mAh g^{-1} at 1000 mA g^{-1}	(196)
Zn_2SnO_4 hollow nanosphere	Hydrothermal method	602 mAh g^{-1} at 100 mA g^{-1}, 60 cycles	442 mAh g^{-1} at 1000 mA g^{-1}	(197)
Hollow Zn_2SnO_4 boxes@C/graphene ternary composite	Hydrothermal process followed by calcination process	726 mAh g^{-1} at 300 mA g^{-1}, 50 cycles	396 mAh g^{-1} at 1800 mA g^{-1}	(198)
Zn_2SnO_4/graphene composite	Hydrothermal method	688 mAh g^{-1} at 200 mA g^{-1}, 50 cycles	300 mAh g^{-1} at 1600 mA g^{-1}	(199)
Hollow Zn_2SnO_4 boxes wrapped graphene	Co-precipitation and electrostatic interaction	678 mAh g^{-1} at 300 mA g^{-1}, 45 cycles	355 mAh g^{-1} at 2000 mA g^{-1}	(200)
Flower-like Zn_2SnO_4 composite	Green hydrothermal synthesis	501 mAh g^{-1} at 300 mA g^{-1}, 50 cycles	-	(201)
PPY coated Zn_2SnO_4	Microemulsion polymerization	478 mAh g^{-1} at 60 mA g^{-1}, 50 cycles	-	(203)
PANI coated Zn_2SnO_4	Emulsion polymerization method	491 mAh g^{-1} at 600 mA g^{-1}, 50 cycles	-	(204)
Ex situ carbon coated Zn_2SnO_4	Hydrothermal synthesis	533 mAh g^{-1} at 700 mA g^{-1}, 50 cycles	-	(212)
Mn doped Zn_2GeO_4 nanosheet array	Hydrothermal synthesis	1301 mAh g^{-1} at 100 mA g^{-1}, 100 cycles	500 mAh g^{-1} at 1000 mA g^{-1}	(233)
Coaxial Zn_2GeO_4@C nanowires	Single-step chemical vapour deposition	790 mAh g^{-1} at 2000 mA g^{-1}, 100 cycles	465 mAh g^{-1} at 10000 mA g^{-1}	(234)
Carbon coated Zn_2GeO_4 on Ni foam	Chemical vapour deposition method	1100 mAh g^{-1} at 400 mA g^{-1}, 1000 cycles	396 mah g^{-1} at 9.6 A g^{-1}	(235)
Ultrathin 2D Co_2GeO_4 Nanosheets	Hydrothermal method	1026 mAh g^{-1} at 0.22 A g^{-1}, 150 cycles	600 mAh g^{-1} at 1.16 A g^{-1}	(29)